

Strain relaxation and dislocations in SiGe/Si structures

P.M. Mooney

IBM Research Division, T.J. Watson Research Center, PO Box 218, Yorktown Heights, NY 10598, USA

Abstract

Epitaxially grown lattice mismatched structures are of increasing importance for microelectronic and optoelectronic devices and circuits fabricated using a variety of semiconducting materials. For some applications, the strain in the epitaxial layers is intentionally relieved by the introduction of misfit dislocations, and the film has an in-plane lattice parameter close to that of the bulk material. For example, a fully relaxed $\text{Si}_{0.7}\text{Ge}_{0.3}$ layer is required as a buffer layer for high mobility field effect transistors having strained Si or strained SiGe channels. In this case it is necessary to control the growth conditions and the design of the structure so as to minimize the density of dislocations threading through device layers grown on top of the relaxed buffer layer.

The need to prevent strain relaxation in thin layers or to control the density and distribution of defects in intentionally relaxed structures has lead to extensive research on strain relaxation mechanisms and on the properties of the defects which are required to relieve the strain. This article will focus on recent work on strain relaxed SiGe/Si structures. Two different relaxation mechanisms occurring at low mismatch strain and low growth temperature will be discussed, and the characteristics of step-graded buffer layer structures will be reviewed. Effects of dislocations on the electronic properties of relaxed SiGe layers will also be discussed.

Keywords: Strain relaxation; Dislocations; Electronic properties

1. Introduction

Epitaxially grown lattice mismatched heterostructures are of increasing importance for microelectronic and optoelectronic devices and circuits. Examples include blue–green lasers fabricated from II–VI semiconductors [1], lasers [2] and high electron mobility transistors (HEMTs) [3] made of III–V semiconductors, and SiGe heterojunction bipolar transistors (HBTs) [4]. In some structures such as SiGe HBTs or III–V semiconductor lasers, the lattice mismatched layers are pseudomorphic to the underlying semiconductor, i.e. they are elastically strained with their in-plane lattice parameter matching that of the underlying material. When the strained layer exceeds a critical thickness, however, the strain is relieved by the introduction of defects and thus the in-plane lattice parameter may be close to that of the bulk semiconductor. Strain relaxed buffer layers are needed for a variety of applications. For example, a fully relaxed $\text{Si}_{0.7}\text{Ge}_{0.3}$ buffer layer is required to serve as a “substrate” for high mobility transistors having strained Si electron channels [5] or strained $\text{Si}_{0.3}\text{Ge}_{0.7}$ [6] or Ge [7,8] hole channels. Also, fully relaxed $\text{Si}_{1-x}\text{Ge}_x$ or Ge buffer layers may be used for integrating optoelectronic devices fabricated from GaAs or other III–V materials with silicon technology. [9] Similarly, strain relaxed InGaAs buffer layers grown on GaAs substrates would allow the use of less expensive GaAs substrates instead of InP substrates for a number of applications, including HEMTs and modulators. [10] These applications require relaxed buffer layers having very low defect densities and excellent electronic and optical properties.

The need to prevent strain relaxation or to control the density and distribution of defects in intentionally relaxed structures has lead to extensive research both on strain relaxation mechanisms, and also on the effects of the defects which are required to relieve the strain on the properties of relaxed semiconductor films. Here we will focus on recent work on strain relaxed $\text{Si}_{1-x}\text{Ge}_x/\text{Si}$ structures in which the maximum lattice mismatch is about 4%. These group IV semiconductors are simpler than

compound semiconductors and thus are the ideal material system in which to investigate relaxation mechanisms and defect properties. At low mismatch strain, $< 1\%$, $\text{Si}_{1-x}\text{Ge}_x$ layers grown on $\text{Si}(001)$ substrates relax by the introduction of 60° dislocations which lie on $\{111\}$ glide planes in the crystal. These dislocations have misfit segments which run in the $\langle 110 \rangle$ directions parallel to the $\text{Si}_{1-x}\text{Ge}_x/\text{Si}$ interface and are terminated by threading arms running up to the surface of the epitaxial structure. The misfit segments relieve strain and are therefore necessary in order to obtain a relaxed $\text{Si}_{1-x}\text{Ge}_x$ layer. In contrast, the threading arms, which do not relieve strain, have deleterious effects on devices. Thus only very low densities of threading arms are acceptable, if these relaxed layers are to be useful “substrates” for electronic or optoelectronic devices.

Epitaxial $\text{Si}_{1-x}\text{Ge}_x$ films are grown by a number of different methods including molecular beam epitaxy (MBE) [9,11] and various chemical vapor deposition techniques including atmospheric pressure chemical vapor deposition (AP/CVD) [12], rapid thermal chemical vapor deposition (RT/CVD) [13] and ultra high vacuum chemical vapor deposition (UHV/CVD) [14]. These growth techniques have all been reported elsewhere and will not be discussed here.

This article reviews recent work on strain relaxed $\text{Si}_{1-x}\text{Ge}_x/\text{Si}(001)$ structures. Results on UHV/CVD-grown material will be emphasized; however, related work on material grown by other methods is included as well. Recent work on high mobility structures and their applications is reviewed in Section 2. Section 3 is a discussion of two different strain relaxation mechanisms observed at low mismatch strain and low growth temperature. The measurement of the thermal activation energy for dislocation nucleation in both these mechanisms is included, as is the importance of step-grading for high quality relaxed buffer layers. The effects of the dislocations needed to relieve the mismatch strain on electron mobility and on the optical and electronic properties of the buffer layers are discussed in Section 4, followed by conclusions in Section 5.

2. High mobility Si/SiGe structures

The achievement of extraordinarily high electron mobility at low temperature in strained Si channels grown on relaxed step-graded $\text{Si}_{0.7}\text{Ge}_{0.3}$ buffer layers demonstrates the high quality of these epitaxial structures and thus their potential for various technological applications [15–18]. This was accomplished by the use of a strained Si quantum well to enhance the electron mobility. The band structure of a semiconductor is modified when the semiconductor is strained [19]. As an example, the conduction band of strained Si is shown schematically in Fig. 1. Strain removes the conduction band

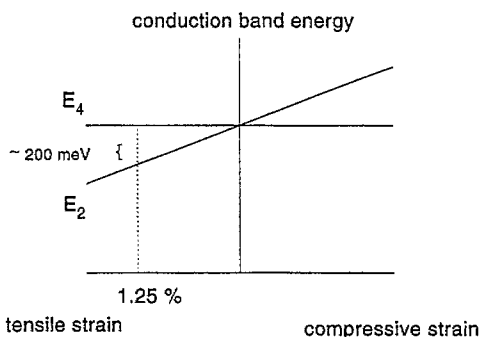


Fig. 1. Schematic diagram of the splitting of the degenerate conduction band valleys in strained Si. Electrons in the valleys labeled E_2 have a light in-plane effective mass and a heavy perpendicular effective mass. Electrons in the valleys labeled E_4 have a heavy in-plane effective mass and a light perpendicular effective mass. The energy difference at a mismatch strain of 1.25%, i.e. for a strained Si layer grown on relaxed $\text{Si}_{0.7}\text{Ge}_{0.3}$ is about 200 meV.

degeneracy and, in the case of tensile strain, the valleys containing electrons having a light in-plane effective mass are at lower energy. Although the band gap of unstrained $\text{Si}_{1-x}\text{Ge}_x$ decreases with increasing x [20], this results primarily from a change in the valence band energy. Thus a thin Si layer, which is grown pseudomorphically on relaxed $\text{Si}_{0.7}\text{Ge}_{0.3}$ and is therefore under tensile strain, forms a quantum well about 200 meV deep for electrons having a light in-plane effective mass, owing to the strain splitting of the conduction band [19].

Fig. 2 shows the structure of UHV/CVD-grown high electron mobility sample [21]. Modulation doping of the strained Si channel is achieved by growing an undoped $\text{Si}_{1-x}\text{Ge}_x$ spacer layer followed by a phosphorous-doped $\text{Si}_{1-x}\text{Ge}_x$ layer on top of the strained Si channel. The electron mobility is a strong function of the measurement temperature, reaching values in the range $3\text{--}4 \times 10^5 \text{ cm}^2 \text{ Vs}^{-1}$ in ungated devices at 0.4 K [15] and as high as $5.2 \times 10^5 \text{ cm}^2 \text{ Vs}^{-1}$ at 0.4 K in gated structures [16] grown by UHV/CVD. High electron mobilities have also been achieved in similar structures grown by MBE [17,18].

Fig. 3 is a plot showing measured values of the low temperature electron mobility in a Si quantum well since the first report in 1985 [22]. The dramatic increase in mobility in the last ten years results from the control of defects in these structures. The order of magnitude increase in mobility to

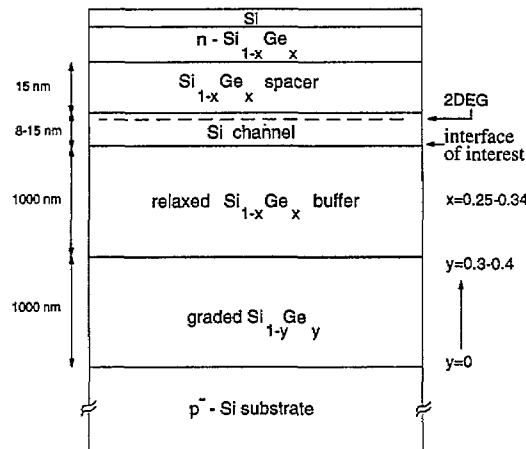


Fig. 2. Layer structure of high electron mobility samples. The Si channel is under tensile strain since it has the same in-plane lattice parameter as the relaxed $\text{Si}_{1-x}\text{Ge}_x$ buffer layer. Electrons from the $\text{n-Si}_{1-x}\text{Ge}_x$ layer transfer to the strained Si quantum well where they form a two dimensional electron gas (2DEG). (From Ref. [21].)

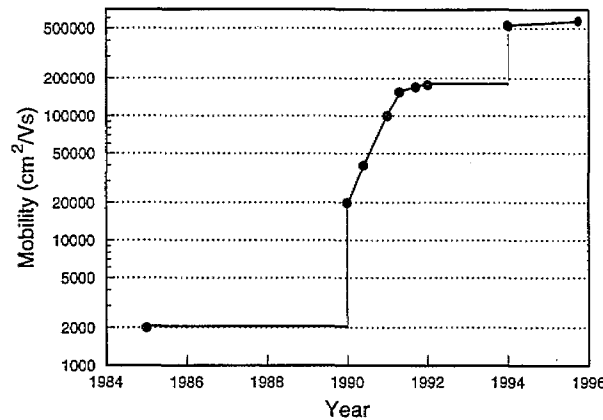


Fig. 3. Plot showing the increase in low temperature electron mobility in the last 10 years. These increases result primarily from the control of dislocations in structures like that shown in Fig. 2.

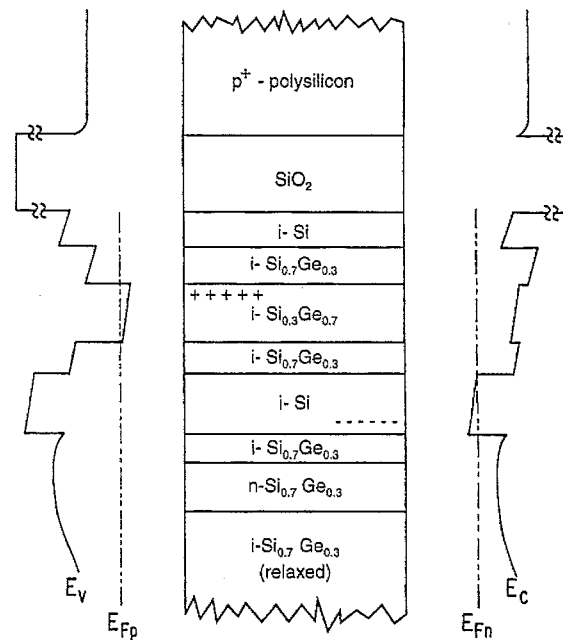


Fig. 4. Layer structure proposed for SiGe CMOS devices. The Fermi level for electrons when the gate is under positive bias is shown at the right; that for holes when the gate is under negative bias is shown at the left. Under positive bias, the strained Si quantum well is occupied by electrons and the n-channel device is on. Under negative bias, the $\text{Si}_{0.3}\text{Ge}_{0.7}$ quantum well is filled with holes and the p-channel device is on. At zero bias, both devices are off. (From Ref. [32].)

$20\,000\text{ cm}^2\text{ Vs}^{-1}$, reported in 1990, resulted from the use of a step-graded relaxed $\text{Si}_{1-x}\text{Ge}_x$ buffer layer, which reduced the density of dislocations threading through the Si channel to values below 10^7 cm^{-2} [23]. During the following two years, improved control of dislocations in the buffer layer structures resulted in another order of magnitude increase in mobility [17,18,24]. The most recent increase in mobility, reported in 1994, was achieved by eliminating misfit dislocations at the buffer layer/channel interface [21]. In addition to defects such as dislocations [25], numerous other factors including the electron density in the Si channel and the thickness of the undoped spacer layer between the Si channel and the n-doped SiGe layer effect the value of low temperature electron mobility [26,27], as do the background charge concentration in the material and interface roughness [28,29]. The very high values of the low temperature electron mobility which have been achieved indicate that all of these factors can be controlled. For example, background doping concentrations in the buffer layers are low enough that they are difficult to measure directly; however, the very high mobility values measured in UHV/CVD-grown structures indicate that the background carrier concentrations $\leq 10^{15}\text{ cm}^{-3}$ [27,30].

Enhancements of the room temperature transport properties can have a significant effect on device performance, especially the ultimate speed. The electron mobility at room temperature in strained Si grown on relaxed $\text{Si}_{1-x}\text{Ge}_x$ at carrier densities required for devices is in the range $2500\text{--}3000\text{ cm}^2\text{ Vs}^{-1}$, about 5 times higher than that of electrons in bulk Si or in CMOS devices [31,32]. A quantum well for holes having a light in-plane mass can be formed by growing a thin compressively strained $\text{Si}_{1-x}\text{Ge}_x$ layer on Si(001) or by growing strained Ge or $\text{Si}_{1-x}\text{Ge}_x$ with high x on relaxed $\text{Si}_{1-x}\text{Ge}_x$ with lower x . The biaxial compressive strain raises the energy of the valence band relative to that of the unstrained alloy (which also increases as x increases) and splits the band so that the light effective mass holes lie at higher energy [33]. The hole mobility at room temperature in the case of strained $\text{Si}_{0.3}\text{Ge}_{0.7}$ grown on relaxed $\text{Si}_{0.7}\text{Ge}_{0.3}$ is about $1000\text{ cm}^2\text{ Vs}^{-1}$, a factor of 3 to 5 higher than the value in p-channel CMOS devices [31,34].

N-channel modulation-doped FETs (MODFETs) fabricated with strained Si on relaxed $\text{Si}_{0.7}\text{Ge}_{0.3}$ were demonstrated several years ago [5]. The higher electron mobility results in a decrease of the sheet resistance of the device in the on state by about a factor of five. In addition, the electric field at which velocity saturation takes place in strained Si is lower than in unstrained Si by about a factor of five. The same velocity can thus be achieved at a much lower field, i.e. at lower bias conditions or in longer channels. More recently p-channel MODFETs fabricated with strained $\text{Si}_{0.3}\text{Ge}_{0.7}$ on relaxed $\text{Si}_{0.7}\text{Ge}_{0.3}$ have also been demonstrated [6]. Gate leakage currents in MODFETs, which are higher in these devices than in Si MOSFETs owing to the use of a Schottky diode gate, can be reduced by the use of a deposited oxide gate, for which a mature technology exists. It has been proposed that n- and p-channel FETs can be integrated, using the layer structure shown in Fig. 4 [31]. Only a single gate is required in this structure; the application of a positive bias allows electrons into the strained Si channel and a negative bias allows holes into the strained $\text{Si}_{0.3}\text{Ge}_{0.7}$ channel.

The structure proposed for SiGe CMOS devices and circuits requires a relaxed $\text{Si}_{0.7}\text{Ge}_{0.3}$ buffer layer to support both the strained Si and $\text{Si}_{0.3}\text{Ge}_{0.7}$ channels. Relaxed $\text{Si}_{1-x}\text{Ge}_x$ buffer layers as “substrates” for III–V optoelectronic devices, such as light emitting diodes [9], and for strain symmetrized superlattices [22] have been demonstrated as well. As will be discussed later on, the requirements for relaxed buffer layers for technological applications are more stringent than for high electron mobility at low temperature. The potential of these applications has stimulated a great deal of work on problems of strain relaxation and defects in this material system.

3. Strain relaxation in SiGe/Si structures

Strain relaxation in epitaxial layers is a classic problem which has been studied for many years. A SiGe layer pseudomorphically grown on a Si substrate is elastically strained, as shown schematically in Fig. 5(a). The in-plane lattice parameter is equal to that of Si, and is thus smaller than the lattice parameter of a bulk SiGe crystal, and the out-of-plane lattice parameter is larger than the lattice parameter of a bulk SiGe crystal. When the film thickness exceeds the critical thickness for pseudomorphic growth, the mismatch strain is relieved by the formation of misfit dislocations, i.e. missing atomic planes in the film as is shown schematically in Fig. 5(b). Early work on strain relaxation focussed on the critical thickness to form dislocations in thermal equilibrium in a strained layer of uniform composition [35–37]. Many of the available substrates had relatively high densities of

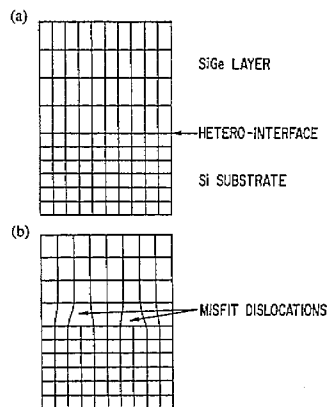


Fig. 5. (a) Schematic diagram of a SiGe layer grown pseudomorphically on a Si substrate. The layer is under compressive strain since it has the same in-plane lattice parameter as the substrate. (b) A partially relaxed SiGe layer in which strain is relieved by misfit dislocations (missing lattice planes).

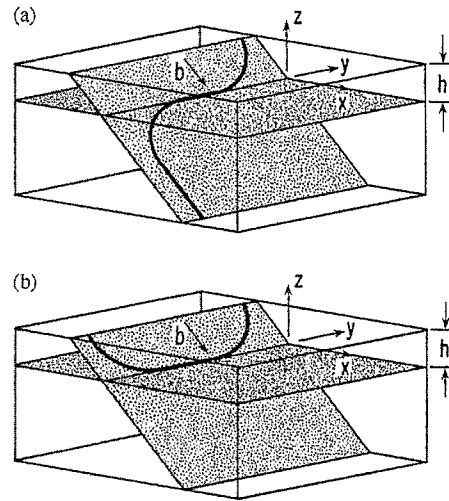


Fig. 6. (a) Schematic diagram of a threading dislocation which has glided in the epitaxial layer to form a misfit segment at the interface. (b) A dislocation half loop formed during growth of the epitaxial layer.

dislocations. Thus the problem considered was the critical thickness required for a dislocation threading from the substrate up through the epitaxial layer to glide, thereby forming a misfit segment at the interface which relieves strain, as shown in Fig. 6(a). With the improvement of bulk-grown semiconductor substrates, especially Si wafers which are now essentially dislocation free even at 8 inch diameter, the nucleation of dislocation loops in the epitaxial layer, as shown schematically in Fig. 6(b), must be considered as well as relaxation by glide of pre-existing threading dislocations.

At low mismatch strain $\text{Si}_{1-x}\text{Ge}_x/\text{Si}(001)$ structures relax by the introduction of 60° dislocations. At low temperatures where diffusion is difficult, and in the absence of non-equilibrium concentrations of point defects, their movement is restricted entirely to glide on $\{111\}$ planes in the crystal [38]. Glide plays an important role in strain relaxation no matter whether dislocations existing in the substrate are grown into the layer or dislocations nucleate in the layer during growth. Glide of 60° dislocations in $\text{Si}_{1-x}\text{Ge}_x$ layers grown on $\text{Si}(001)$ substrates has been studied extensively by two different methods [39–42]. Both involve growing metastable strained layers, which are thicker than the equilibrium critical thickness for strain relaxation, in which relaxation is kinetically limited by the low growth temperatures and short growth times for these films. In one method, the strained samples were annealed in the temperature range from 550 to 950 °C and subsequently etched. Afterwards the length of the misfit segments was measured by means of an optical microscope with interference (Nomarsky) contrast [39,40]. The length and density of the misfit segments was found to increase with increasing annealing temperature. The thermally activated glide velocity is given by [43]

$$v_g = B \epsilon \exp(-E_g/kT) \quad (1)$$

where v_g is the glide velocity, ϵ is the mismatch strain, E_g is the thermal activation barrier for glide and B is a constant. Since the annealing time was known, the glide velocity at each temperature was determined and, from this, the thermal activation energy for glide could be calculated. The activation barrier for glide was found to be $E_g = 2.5 \pm 0.2$ eV, with no systematic dependence on the alloy composition, in one experiment [40]. In another, the activation barrier was found to vary with the alloy composition as $E_g = (2.16 - 0.7x)$ eV [39]. The latter results are in good agreement with the values measured in bulk Si (2.2 eV) and bulk Ge (1.6 eV).

Glide has also been observed in real time by cross-sectional transmission electron microscopy (TEM) [41,42]. Metastable strained layers were thinned for TEM measurements and were then

annealed in-situ in the TEM. Measurements of the glide velocity were made during annealing using a video camera, and additional images were also taken after annealing. Similar values of the glide activation energy, $E_g = (2.2-0.6x)$ eV, were found in the TEM experiments and were shown to be consistent with the diffusive double kink model [44] for dislocation glide [41,42].

With the increased use of low temperature epitaxial growth techniques, it has been realized that strain relaxation is kinetically limited [41,45] and that dislocation nucleation in the epitaxial film may be the limiting step in strain relaxation. At low mismatch strain ($< 1\%$), homogeneous nucleation of dislocations cannot occur during growth at the growth rates and temperatures typically used in the laboratory [46–50]; however, dislocation nucleation occurs at defects [49,51] or by multiplication of pre-existing dislocations [52–54]. Alternatively, dislocation nucleation may also occur via surface roughening [55–59]. In uniform composition $\text{Si}_{1-x}\text{Ge}_x$ layers grown by UHV/CVD on Si(001) substrates relaxation occurs either by dislocation multiplication or by dislocation nucleation via surface roughening, depending on the mismatch strain and growth temperature. Relaxation by dislocation multiplication is preferred, since this mechanism yields layers with the low densities of threading dislocations and flat surfaces required for technological applications [53].

3.1. Strain relaxation mechanisms

Dislocation multiplication by a modified Frank-Reed mechanism (MFR) was first observed in compositionally graded layers and is also found in uniform composition layers when the Ge mole fraction is < 0.2 [53,60,61]. It was proposed that intersections of pre-existing misfit dislocations, which run in two perpendicular $<110>$ directions at the substrate epi-layer interface, act as Frank-Reed sources for dislocation multiplication [53]. A characteristic feature of this mechanism is dislocation pile-ups several microns deep in the Si substrate as shown in Fig. 7, which is a cross sectional TEM image of a relaxed $\text{Si}_{0.85}\text{Ge}_{0.15}$ layer. It was suggested that the interaction of the two perpendicular dislocations having the same Burgers vector forms two corner dislocations, each one having misfit

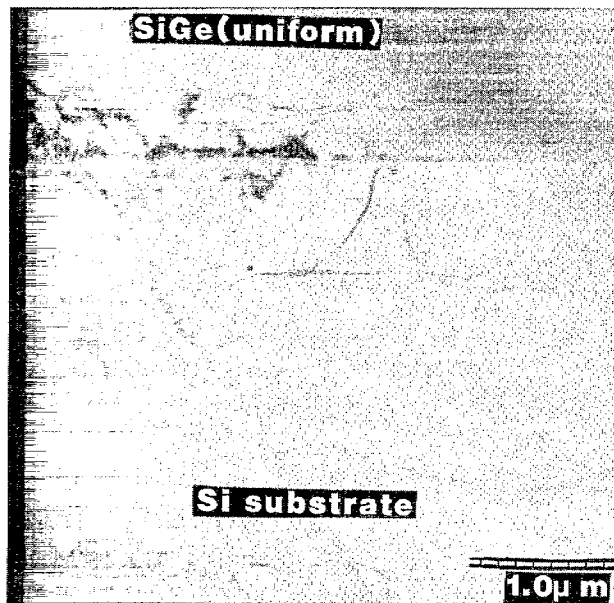


Fig. 7. Cross sectional TEM image of a UHV/CVD-grown $\text{Si}_{0.85}\text{Ge}_{0.15}$ layer on a Si(001) substrate. The dislocation pile-up deep in the substrate is typical of the MFR mechanism. (From Ref. [74].)

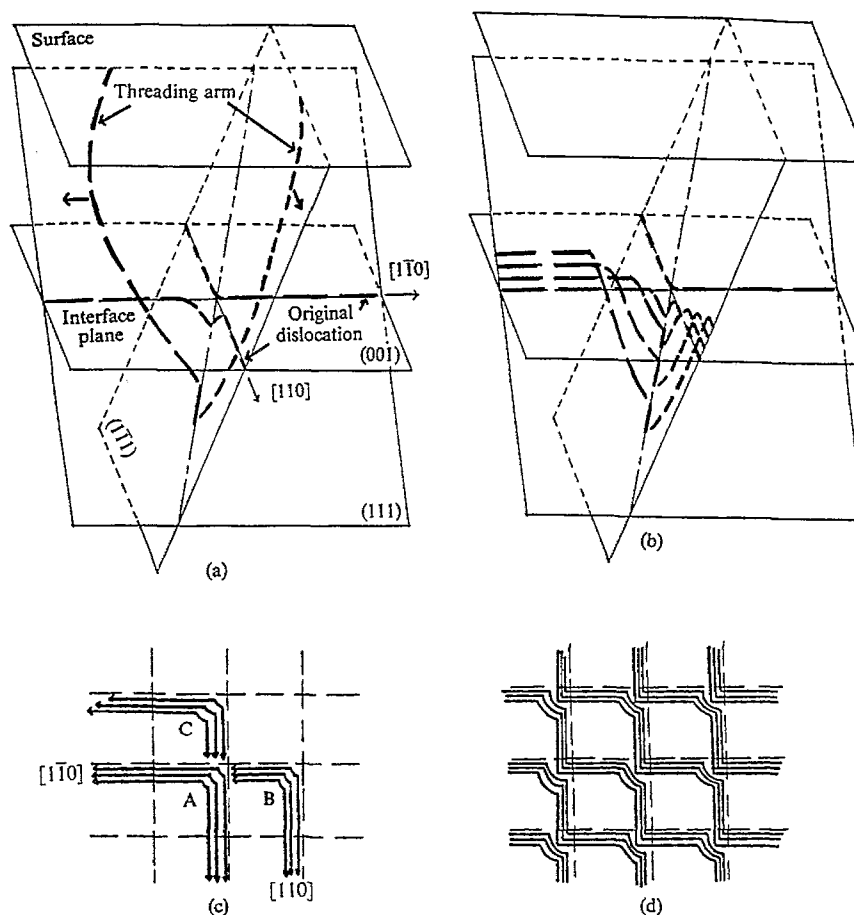


Fig. 8. (a) and (b) Schematic diagrams showing the evolution of a dislocation pile-up in the MFR mechanism. The original dislocations interact forming two corner dislocations which act as Frank-Read sources for dislocation multiplication. (c) and (d) Planar view schematic diagrams showing the annihilation of threading dislocations (B and C) resulting in very long misfit segments and low threading dislocation densities. (From Ref. [61].)

segments running in the two perpendicular $\langle 110 \rangle$ directions and thus lying on two different $\{111\}$ glide planes. A small half loop forms on one of the corner dislocations, which grows by glide to relieve the excess stress in the epitaxial layer as shown in Fig. 8(a) [53,61]. When the upper part of the loop reaches the sample surface, the threading arms continue to glide as described above. Typically there is enough excess stress that this process occurs repeatedly, thus forming a double pile-up of corner dislocations having the same Burgers vector on the same two glide planes as shown in Fig. 8(b). The repulsive force between identical dislocations on the same glide plane pushes the misfit segments down into the Si substrate. This multiplication process repeats until sufficient strain is relieved. Since this mechanism can occur only when the pinning points of the Frank-Read sources are sufficiently far apart, it is observed only when the pre-existing dislocations occur at very low densities. Since these "original dislocations" nucleate at defects or particulates at the layer/substrate interface, this mechanism occurs only under very clean growth conditions [53].

In addition to the dislocation pile-ups deep in the Si substrate, another important feature of this mechanism is the low density of threading dislocations which results. This is believed to result from the annihilation of the threading segments which apparently glide over large distances [61]. As shown in Fig. 8(c) and (d), the network of pre-existing dislocations acts as a set of self-aligned sources,

making large-scale annihilation possible and reducing the threading dislocation densities by many orders of magnitude compared with other relaxation mechanisms [61]. Dislocation glide is critically important in this mechanism, as is indicated by both the low density of threading arms and the very large dislocation loops in the substrate. This suggests that the rate limiting step in the relaxation process is nucleation and that the activation barrier for dislocation nucleation by this mechanism must be larger than that for glide.

A competing mechanism for strain relaxation is the modulation of the surface profile or surface roughening. This type of surface roughening (not to be confused with thermal roughening of the surface) is caused by the growth of coherently strained islands or clusters. Although it increases the surface area, this growth mechanism allows partial relaxation of the strain in the film by elastic deformation [58,62]. This type of surface roughening can take the form of sharp grooves or pits in the surface [57], providing regions of large stress where the thermal activation barrier to dislocation nucleation is extremely small [59]. It has been shown that the thermal activation barrier for surface roughening depends on the mismatch strain as ϵ^{-4} [58], whereas the activation barrier for dislocation nucleation by other mechanisms typically varies as ϵ^{-1} . Dislocation nucleation via surface roughening is therefore favored at larger mismatch, whereas the MFR mechanism is favored at smaller mismatch.

Fig. 9 shows TEM cross-sectional micrographs of $\text{Si}_{1-x}\text{Ge}_x$ layers of $x=0.15$ and $x=0.30$ grown by UHV/CVD at 560 °C. The $x=0.15$ layers shown in (a) and (b) have smooth surfaces and clearly relax by the MFR mechanism. In contrast, $x=0.30$ layers shown in (c) and (d), which were grown at the same temperature, have rough surfaces. Dislocation nucleation occurs subsequent to surface roughening as seen in the thicker film. Clearly, the activation barrier for roughening and subsequent dislocation nucleation was lower in the $x=0.30$ films than the barrier for dislocation multiplication, although the opposite was true in the $x=0.15$ films. For these films the silane flow rate was constant and the germane flow rate was varied to give the desired alloy composition in the film. In the UHV/CVD technique the growth rate of the film increases with the Ge flow rate and decreases with growth temperature. Thus effects of growth rate were not investigated independently; they are coupled with changes in alloy composition and growth temperature in this experiment.

Fig. 10 is a plot showing the conditions of mismatch strain and growth temperature at which the strain is relieved by each of these two dislocation nucleation mechanisms in UHV/CVD-grown layers. At each growth temperature, there is a critical strain above which surface roughening is observed. At a given mismatch strain, lowering the growth temperature reduces the surface mobility of the adatoms, thus suppressing surface roughening and allowing relaxation by MFR mechanism.

Atomic force microscopy measurements show the very different surface morphology of films which relax by these two mechanisms. Fig. 11(a) is an image of the surface of the sample of Fig. 9(d). The $\text{Si}_{0.7}\text{Ge}_{0.3}$ layer was grown at 560 °C and is on average about 50 nm thick. This image shows not only that the amplitude of the roughness is relatively large (70 nm), but also that the surface is faceted [63]. Fig. 11(b) shows the surface morphology of a uniform composition $\text{Si}_{0.7}\text{Ge}_{0.3}$ film grown at 500 °C, which relaxed by the MFR mechanism. As is typical of samples which relax by this mechanism, there is a clear cross-hatch pattern, with ridges running in the $\langle 110 \rangle$ directions, i.e. in the same directions as the misfit dislocations which lie well below the sample surface. In these films the cross hatch pattern arises from the surface steps formed by the 60° dislocations, either single dislocations when the layer is very thin and only a small fraction of the strain is relieved, or dislocation pile-ups in thicker substantially relaxed films [64,65]. In both cases the surface morphology is consistent with that expected solely from such steps, and the amplitude of the cross-hatch in the growth direction is much smaller than when samples relax by surface roughening. The cross-hatch surface morphology was suggested to arise from lateral non-uniformities in the strain field of the misfit dislocations in MBE-grown structures grown at much higher temperature [9]. Which of these two possible mecha-

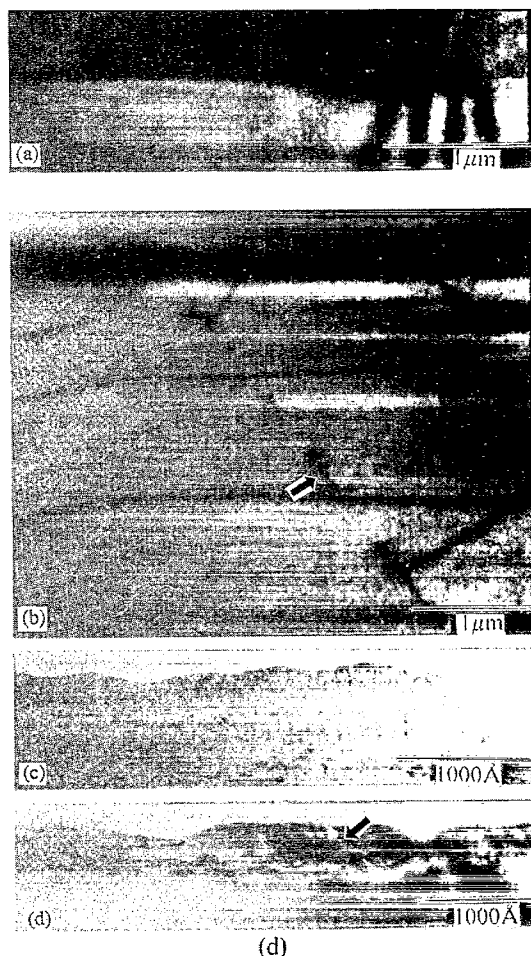


Fig. 9. Cross sectional TEM images of samples grown by UHV/CVD at 560 °C: (a) a strained $\text{Si}_{0.85}\text{Ge}_{0.15}$ with a flat surface; (b) a thicker $\text{Si}_{0.85}\text{Ge}_{0.15}$ layer partially relaxed by the MFR mechanism; (c) a $\text{Si}_{0.7}\text{Ge}_{0.3}$ layer which has partially relaxed by surface roughening; and (d) a thicker $\text{Si}_{0.7}\text{Ge}_{0.3}$ layer which initially relaxed by surface roughening and then further relaxed by the introduction of misfit dislocations. (From Ref. [58].)

nisms is more important apparently depends on the growth conditions. Note that the length scale of the cross hatch pattern in the in-plane direction is much larger than that of the faceted roughness.

Fig. 12 shows cross sectional TEM images of a uniform composition $\text{Si}_{0.75}\text{Ge}_{0.25}$ layer and a step-graded layer both grown at 560 °C. The uniform layer relaxed by roughening and subsequent random nucleation of dislocations; however, the graded layer relaxed by the MFR mechanism. At this growth temperature, uniform $\text{Si}_{0.85}\text{Ge}_{0.15}$ layers relax by dislocation multiplication, owing to the lower mismatch strain (see Fig. 10). We therefore infer that dislocation nucleation in graded structures begins while the lower x regions are growing. Sufficient strain is relieved prior to the growth of the higher x layers that surface roughening is suppressed and relaxation occurs by the MFR mechanism. This results in high quality films, i.e. films having relatively flat surfaces and low threading dislocation densities, at alloy compositions required for device applications.

High quality $\text{Si}_{1-x}\text{Ge}_x/\text{Si}$ buffer layers have also been grown under different conditions by other growth methods. Examples are step-graded layers grown at 800 °C by RT/CVD [66,67], and at temperatures ranging from 700 to 900 °C by MBE [9]. Recently, step-graded buffer layers with very low threading dislocation densities have been achieved by growing each $\text{Si}_{1-x}\text{Ge}_x$ step by AP/CVD

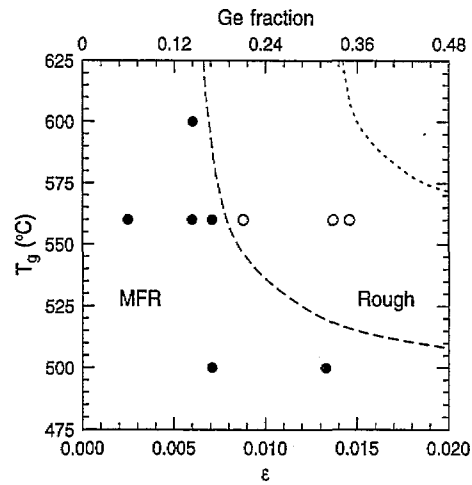


Fig. 10. Plot showing the conditions at which uniform composition $\text{Si}_{1-x}\text{Ge}_x$ layers grown by UHV/CVD relax by different mechanisms. Open circles indicate relaxation via surface roughening and solid circles indicate relaxation by the MFR mechanism.

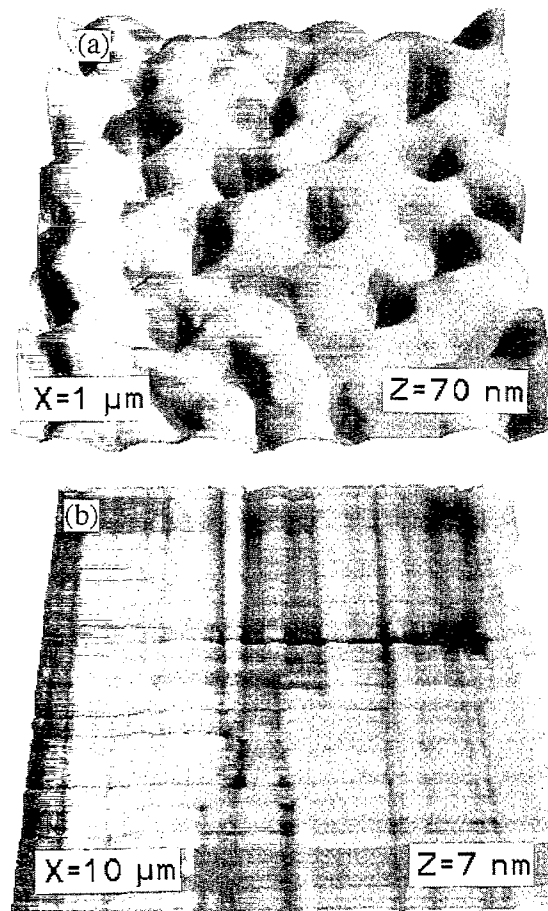


Fig. 11. AFM images of the surfaces of uniform composition $\text{Si}_{0.7}\text{Ge}_{0.3}$ layers: (a) relaxed via surface roughening and (b) relaxed by the MFR mechanism. (From Ref. [63].)

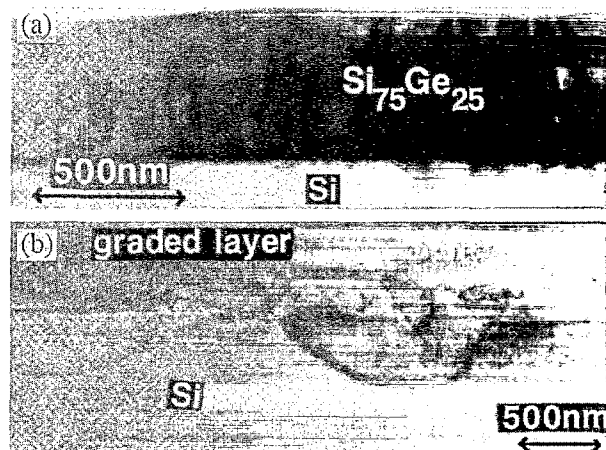


Fig. 12. Cross sectional TEM images of structures grown by UHV/CVD at 560 °C: (a) a uniform composition Si_{0.75}Ge_{0.25} layer and (b) a layer graded continuously up to Si_{0.75}Ge_{0.25}. (From Ref. [53].)

at low temperature, i.e. under growth conditions where the layer remains strained, and then annealing it in-situ at high temperature (> 1000 °C) for 1 h to relieve the strain [68]. At this high temperature, dislocations nucleate at the wafer edge and glide all the way to the opposite edge of the wafer. Once a step has relaxed, the lattice mismatch during growth of the next higher x step is reduced. Therefore this sequence can be repeated until the desired in-plane lattice parameter is achieved. A method for the controlled nucleation of dislocations using ion implantation to create nucleation sources at specified locations has also been proposed [69]. Since different nucleation sources are active at different growth or annealing temperatures, the mechanism of dislocation nucleation is different in the various schemes just described. However, dislocation glide is clearly important in all of these strain relaxation mechanisms, as is evident from the low threading dislocation densities.

3.2. Dislocation nucleation activation energy

In the MFR relaxation mechanism discussed above, the rate limiting step is dislocation nucleation. In contrast, when the layer relaxes by roughening and subsequent random nucleation, threading dislocation densities are very high, suggesting that nucleation occurs more readily than dislocation glide. The barrier for dislocation nucleation has been determined for both these mechanisms from high resolution X-ray diffraction measurements of relaxed SiGe layers grown by UHV/CVD.

High resolution X-ray diffraction is a powerful analytical technique to quantify strain relaxation in both uniform composition and step-graded epitaxial layers. This technique allows the precise measurement of the lattice parameter of an epitaxial film, which often differs from that of the substrate by only a fraction of a percent. The usual approach is to make rocking curve measurements using a symmetric reflection, the 004 reflection when the substrate is Si(001), from which the out-of-plane lattice parameter is calculated using Bragg's law [70]. Provided the relation between lattice parameter and alloy composition is known, the symmetric reflection is sufficient to determine the alloy composition of a fully strained layer, since the in-plane lattice parameter is the same as that of the substrate in that case. Whether or not the layer has relaxed can be seen from the shape of the diffraction peak, which is broadened when defects are present; however, this measurement is not very sensitive to low densities of defects, i.e. to the initial stages of strain relaxation [71]. To evaluate a relaxed layer, it is necessary to measure an asymmetric reflection as well, i.e. diffraction from planes at an angle to the sample surface. The separation of such planes can be expressed in terms of the in-plane and out-of-

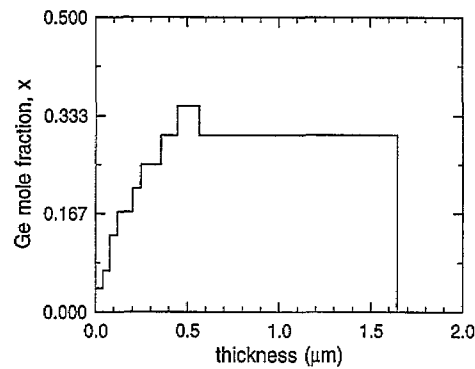


Fig. 13. The Ge profile of a UHV/CVD-grown structure having a step-graded layer and a uniform composition cap layer.

plane lattice parameters, thus allowing both the alloy composition and the degree of relaxation of the film to be determined [70].

Rocking curve measurements are useful to evaluate uniform composition layers and also graded structures where the layer of interest is thick compared with the graded region of the structure, e.g. the top layer of the structure shown in Fig. 13. More sophisticated “triple-axis” measurements, in which the acceptance angle of the detector is greatly reduced by the use of an analyzing crystal [71], allow the variation in lattice parameter of the layer to be distinguished from the bending of the lattice planes, referred to as mosaic structure, owing to the presence of dislocations or other defects. Using this technique the diffraction peaks of the individual steps in a step-graded structure can be resolved, provided the layers are sufficiently thick that each has a well-defined lattice constant [72].

X-ray diffraction measurements of both step-graded structures similar to that in Fig. 13, and also uniform composition layers, showed that epitaxial layers which relax by the MFR mechanism have a large crystallographic tilt with respect to the Si substrate when they are grown on miscut substrates [73,74]. X-ray rocking curves of a step-graded structure with a $3.5 \mu\text{m}$ thick $x=0.30$ layer on top of a $0.6 \mu\text{m}$ thick step-graded layer are shown in Fig. 14. Data was taken with the sample in four different orientations in the plane of the wafer. The very intense narrow peak is the 004 reflection from the Si substrate and the broader less intense peak is that from the thick SiGe cap layer. The angle plotted (ω) is the position of the sample holder. The shifting of the Si peak as the sample is rotated in the plane of the wafer indicates that the wafer is miscut, i.e. that the surface of the wafer is not parallel to the (001)

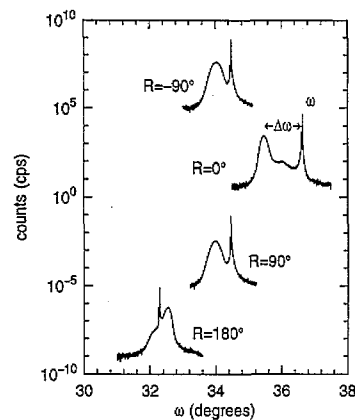


Fig. 14. High resolution X-ray rocking curves of a sample having a $0.6 \mu\text{m}$ thick step-graded layer and a $3.5 \mu\text{m}$ thick cap layer. The parameter R indicates the orientation of the plane of the wafer with respect to the diffraction plane. ω is the angle between the sample holder and the incident X-ray beam. (From Ref. [74].)

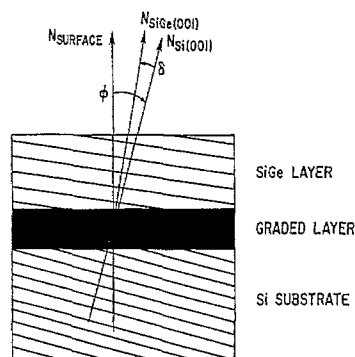


Fig. 15. Schematic diagram showing the miscut angle (ϕ) of the Si substrate and the tilt angle (δ) between the (001) lattice planes of the substrate and the SiGe layer. (From Ref. [74].)

lattice planes. The miscut angle is determined from the extreme values of ω [70,72], at $R=0^\circ$ and 180° in this case, and is about 2° for this wafer. What was surprising about this data is that the peak separation, $\Delta\omega$, also varies as the sample is rotated. In fact, the variation is so large that the layer peak, which is expected to occur at a lower angle than the substrate peak, shifts to an angle larger than the substrate peak at $R=180^\circ$. The tilt angle, determined from the extreme values of the peak splitting which also occur at $R=0^\circ$ and 180° [74], is about 0.6° . Fig. 15 shows schematically the orientation of the (001) lattice planes with respect to the sample surface. Note that the layer is tilted in the direction which reduces the angle between the (001) planes and the sample surface.

A large tilt angle is evidence of preferential dislocation nucleation [73,74]. When the (001) lattice planes are parallel to the sample surface, equal densities of dislocations are nucleated on all glide planes and their tilt components cancel out. However, when the substrate is miscut, there is a net tilt, because more dislocations are nucleated on some glide planes than on others. Preferential nucleation is clearly demonstrated in the cross sectional TEM images of two structures step-graded to $x=0.30$ which were grown simultaneously on two different substrates in Fig. 16 [73]. The upper image of the

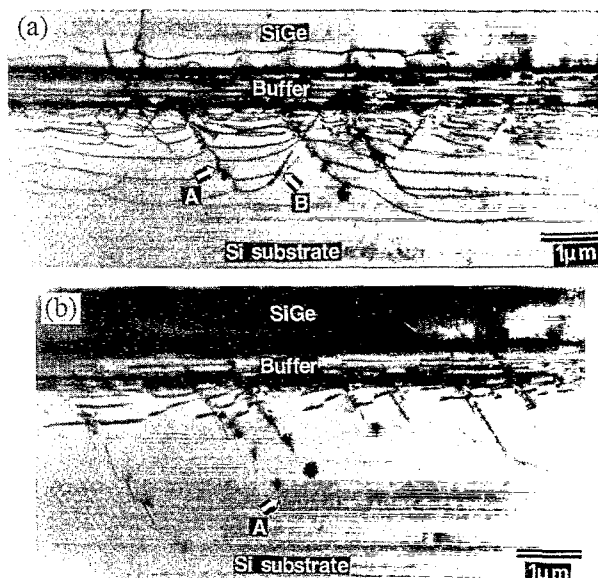


Fig. 16. Cross sectional TEM images of a structure step-graded to $\text{Si}_{0.7}\text{Ge}_{0.3}$ grown on (a) a substrate with negligible miscut and (b) a substrate miscut by 2° . (From Ref. [73].)

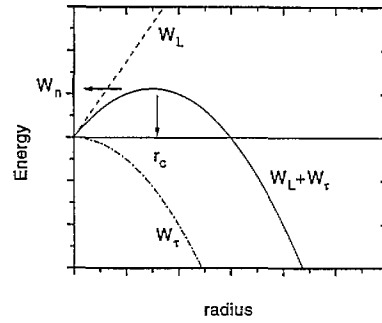


Fig. 17. Schematic diagram showing the thermal activation barrier for dislocation nucleation. The dashed curve indicates the energy of the dislocation loop. The dashed/dotted curve indicates the energy decrease owing to the strain relieved by the dislocation loop. The solid line is the total of these two energies. The nucleation barrier is the maximum of the total energy at the critical radius, r_c .

structure on a substrate with negligible miscut shows dislocation pile-ups oriented in two different directions in roughly equal numbers, whereas the lower image of the structure on a 2° miscut substrate shows pile-ups primarily in only one direction. The driving force for dislocation nucleation is to reduce the total energy by relieving strain. Because the angles between the different glide planes and the surface are not all equal when the substrate is miscut, however, the projections of the misfit components of the Burgers vector of dislocations on different planes are unequal [73,74]. Thus more strain is relieved by each dislocation on the glide planes where the projection of the misfit component is larger.

When the angles between the wafer surface and the four $\{111\}$ glide planes are not all equal, the resolved shear stress is unequal on the four glide planes. The resolved shear stress has a linear effect on the dislocation glide velocity [42,43], but it clearly has a much greater effect on dislocation nucleation. Assuming that the resolved shear stress has an exponential effect on nucleation, i.e. that it effects the nucleation barrier, then measurements of the variation of the tilt angle with the miscut angle can be used to determine the dislocation nucleation barrier [74,75].

Dislocation nucleation is a thermally activated process because, although the dislocation relieves strain and thus reduces the energy of the layer, the formation of the dislocation increases the energy. Following Ref. [47], the self-energy of a loop of radius r and Burgers vector $(a/2)$ $[101]$ gliding on the $(11\bar{1})$ plane, W_L , is proportional to r . The strain energy relieved by the formation of the loop, W_r , is proportional to $-r^2$. The activation energy is found by maximizing the total energy, $W_L + W_r$, with respect to r to determine the critical radius r_c . The activation energy, W_n , is the value of the total energy at r_c , as shown schematically in Fig. 17. This energy can be approximated by

$$W_n = K/\epsilon_n \sin\theta \cos\theta \quad (2)$$

where K is a constant which includes the materials parameters, ϵ_n is the mismatch strain at which nucleation occurs and θ is the angle between the glide plane and the surface, which depends on the miscut angle [74]. The term $1/\sin\theta \cos\theta$ is called the Schmidt factor. Assuming that the dependence on these variables is the same for the MFR mechanism as for homogeneous nucleation [74,75], the nucleation barrier will have the same functional form as Eq. (2), but a different value for the constant, which can be determined from the experimental data for the variation of the tilt angle with the miscut angle.

There are four slip systems for the corner dislocations formed in MFR mechanism, as shown in Fig. 18. It was found experimentally that the tilt angle is in the direction opposite to the miscut angle [74]. In the case of a substrate which is miscut toward $[101]$, the effects of the miscut cancel out on the two slip systems labeled MFR1 and MFR4. The activation barrier is increased or decreased on

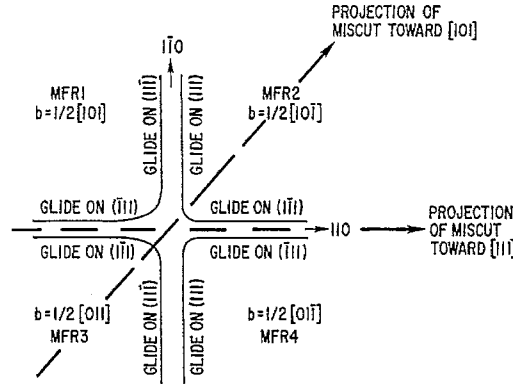


Fig. 18. Schematic diagram showing a planer view of the four slip systems of the corner dislocations in the MFR mechanism. (From Ref. [74].)

MFR2 and MFR3. It was shown that the tilt angle, δ , depends on the total amount of relieved strain, ϵ^* , and the nucleation barriers W_2 on MFR2 and W_3 on MFR3 as follows [74]:

$$\tan \delta = \epsilon^* \frac{b_{\text{tilt}}}{b_{\text{misfit}}} \sqrt{2} \left[\frac{\exp(-\Delta W_3/kT) - \exp(-\Delta W_2/kT)}{2 + \exp(-\Delta W_3/kT) + \exp(-\Delta W_2/kT)} \right] \quad (3)$$

where b_{misfit} and b_{tilt} are the misfit and tilt components of the Burgers vector. Note that since the tilt angle is small, $\tan \delta \propto \delta$. Thus δ varies linearly with ϵ^* , the relieved strain. The term in brackets contains the activation energies, which vary with the miscut angle of the substrate according to Eq. (2).

Fig. 19 shows the variation of the tilt angle with the miscut angle for two groups of samples, all having $x \approx 0.3$ and a relieved strain, which is proportional to the density of misfit dislocations, of $\epsilon_* = 0.012 \pm 0.001$ [74,75]. The solid circles are data for samples which relaxed by the MFR mechanism and have tilt angles increasing with the miscut angle up to about 0.8° . The open circles are uniform composition layers which relaxed by roughening and subsequent random nucleation of dislocations and have tilt angles $< 0.05^\circ$. The large difference in the tilt angles for these two groups of samples indicates that the dislocation nucleation barrier in these two mechanisms is very different. The dotted curve in Fig. 19 was found assuming a nucleation activation barrier of 40 eV, the value previously calculated for homogeneous nucleation of a full loop [47]. The data points for samples

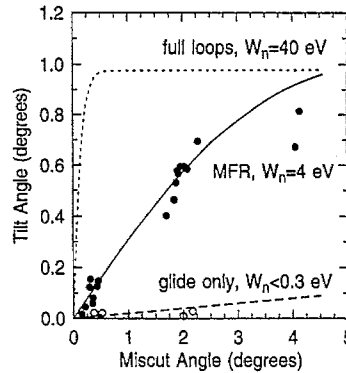


Fig. 19. Plot of the tilt angle vs. the miscut angle for $\text{Si}_{0.7}\text{Ge}_{0.3}$ layers relaxed by the MFR mechanism (solid circles) and via surface roughening (open circles). The relieved strain in these structures was $\epsilon^* = 0.012 \pm 0.001$. The dotted line is the calculation for full loops in a single uniform $\text{Si}_{0.7}\text{Ge}_{0.3}$ layer. The solid line is for $K/\epsilon_n = 26 kT$ in Eq. (2), which gives a value for W_n of 4.0 ± 0.5 eV for MFR relaxation. The dashed line is a calculation assuming that the miscut does not affect nucleation, but only glide.

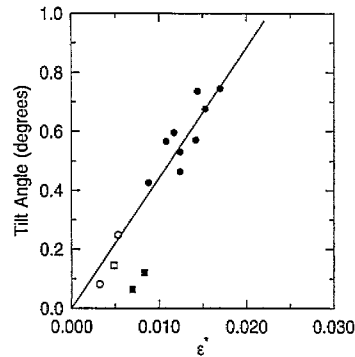


Fig. 20. Plot of the tilt angle vs. relieved strain for structures grown on substrates having a miscut angle of $2.0 \pm 0.2^\circ$. The solid line is calculated for $W_n = 4.0$ eV, assuming that ϵ_n is the same in all samples. Solid symbols are step-graded structures and open symbols are for uniform composition layers. Circles are for samples grown by UHV/CVD at 560°C and squares are for samples grown by AP/CVD as described in the text.

relaxed by the MFR mechanism fall well below this curve as expected. The solid curve is a fit to these data points and gives an activation barrier of 4 eV for the nucleation activation barrier in this mechanism. This value is reasonable and, as expected, it is larger than the activation barrier of 2 eV for dislocation glide. The dashed curve was calculated assuming that the substrate miscut has no effect on dislocation nucleation and only effects glide; in this case the activation barrier for nucleation must be < 0.3 eV. The data for samples which relax via surface roughening fall close to this curve, confirming that the activation barrier for roughening and subsequent dislocation nucleation in these samples is negligibly small, much smaller than that for dislocation glide.

Fig. 20 is a plot of the variation of the tilt angle of the relaxed layer with the relieved strain for samples grown on substrates having miscut angles of $2.0 \pm 0.2^\circ$. As expected from Eq. (3), the tilt angle varies linearly with the relieved strain for the UHV/CVD-grown samples. Data for AP/CVD layers is included on this plot. The tilt angle of a $\text{Si}_{0.83}\text{Ge}_{0.17}$ layer grown at 575°C by AP/CVD is similar to those measured in comparable layers grown by UHV/CVD, confirming that this AP/CVD-grown layer also relaxed by the MFR mechanism. In contrast, two step-graded samples grown in the same week in the same AP/CVD reactor, but at temperatures which decreased with increasing Ge mole fraction from 800°C (when $x = 0.03$) down to 575°C (when $x = 0.22$), had tilt angles much smaller than comparable step-graded layers grown by UHV/CVD entirely at 560°C . The much smaller tilt angle is indicative of a lower dislocation nucleation barrier, suggesting that dislocations nucleate by some other mechanism in these AP/CVD-grown structures, owing to the much higher growth temperatures used for the low x steps. This result demonstrates that the MFR mechanism occurs only at relatively low growth temperatures [76].

The nucleation barrier for the MFR mechanism and that for nucleation via roughening are plotted as a function of strain in Fig. 21. Since the strain decreases as the structures relax, the value of 4 eV determined from the tilt angle measurements in samples grown at 560°C is clearly an average value. The average strain at which nucleation occurs and the range were determined from the data for uniform composition layers grown at the same temperature (Fig. 10). The vertical error bar was determined from the scatter in the measured tilt angles (Fig. 19). The solid curve passing through this data point shows the mismatch strain dependence of the nucleation barrier for the MFR mechanism, which varies as ϵ^{-1} . The dashed curve shows the variation of the nucleation barrier for roughening, which varies as ϵ^{-4} . This curve was plotted so as to cross the curve for the MFR mechanism at $x = 0.19$, the crossover composition determined from the data for uniform layers in Fig. 10. At higher Ge mole fraction the barrier for relaxation by roughening is lower than for relaxation by MFR multiplication, and below

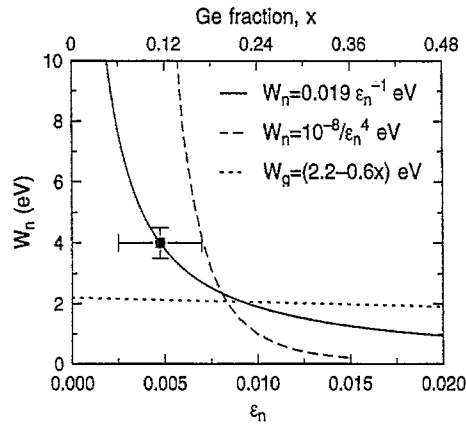


Fig. 21. Plot of the activation barrier vs. strain for dislocation nucleation by the MFR mechanism (solid curve) and for surface roughening (dashed curve). The data point is the nucleation barrier measured for relaxed step-graded structures grown at 560 °C, with the range of ϵ_n determined from the data in Fig. 10. The crossing point for the two curves was also determined from the data in Fig. 10. The activation barrier for glide (dotted curve) is included for comparison.

the crossover composition the barrier for relaxation by the MFR mechanism is lower than that for roughening. The activation barrier for dislocation glide is plotted as a dotted curve in Fig. 21. In the range of mismatch strain where the MFR mechanism occurs, the activation barrier for glide is lower than for nucleation. The lower the mismatch strain at which nucleation occurs, the more likely it is that an existing dislocation will glide. Thus one would expect increased annihilation of threading dislocations in such structures.

Up to this point we have discussed strain relaxation in $\text{Si}_{1-x}\text{Ge}_x/\text{Si}(001)$ structures in terms of 60° total dislocations. Although this is often useful, there are instances when it is important to remember that such defects are energetically unstable with respect to dissociation into a 30° and a 90° Shockley partial dislocation separated by a stacking fault. For $\text{Si}_{1-x}\text{Ge}_x$ grown on $\text{Si}(001)$, the defect moves as a very narrowly dissociated total dislocation [42]. It was recently realized that the Schmidt factor for the 90° partial dislocation was used inadvertently in Eq. (2) instead of that for the 60° dislocation. The relation between the nucleation barrier and tilt angle was also derived using the Schmidt factors both for the 60° total dislocation and for the 30° partial dislocation. However, only the Schmidt factor for the 90° partial dislocation gives results which are consistent with the experiment [77]. A similar result was reported recently for relaxed InGaAs layers grown on GaAs(001) substrates [78]. This is not surprising, since the strain relaxation mechanisms are apparently similar to those for SiGe [79]. The tilt angle, measured in this case by TEM rather than by X-ray diffraction, was used to determine the nucleation activation barrier for dislocations in relaxed InGaAs/GaAs structures. In this material system also, only the geometry of the 90° partial dislocation is consistent with the data [78]. This does not effect the value obtained for the nucleation activation barrier. It does, however, make the interpretation of the nucleation event more complicated. Both these experiments show that the rate limiting step must be nucleation of the 90° partial dislocation. It was suggested that the 30° partial dislocation and the stacking fault are formed by athermal processes [78]. Further work is needed to understand this complex process at the microscopic level.

Reciprocal space mapping [71] is even more powerful than X-ray rocking curves for the study of relaxed epitaxial structures. Rocking curves like those in Fig. 14 do not allow variations in lattice parameter caused by non-uniformities in alloy composition or strain relaxation to be distinguished from the local tilting of the lattice planes caused by the presence of defects, since both effects contribute to the width of the diffraction peak. These effects can be separated by placing an analyzer crystal in

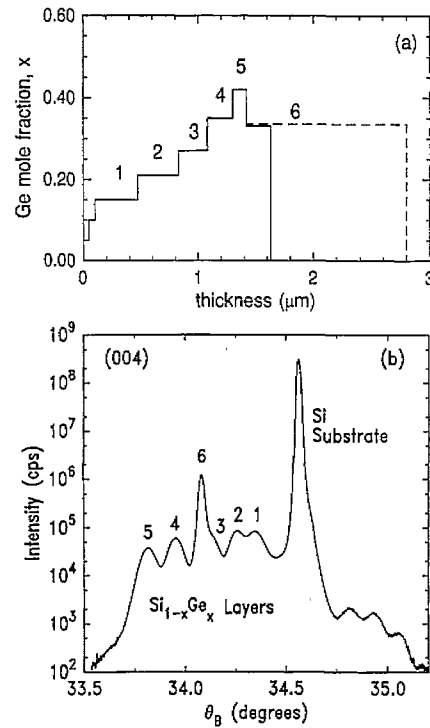


Fig. 22. (a) Ge profiles of two samples having the same step-graded layer sequence but cap layers of different thickness. (b) Triple-axis X-ray spectrum for the sample in (a) with the thicker cap layer. X-ray peaks are numbered to indicate the corresponding layer in the sample.

front of the detector. The analyzer has a very small acceptance angle; thus the detector position (2θ) is very precisely determined. Variations in Bragg angle, θ_B , are measured by $\omega/2\theta$ scans in which the detector moves at twice the rate of the sample holder. With the analyzer in place, only diffraction from regions of the relaxed layer having parallel lattice planes are detected. Any variation in the tilt of the lattice planes, sometimes referred to as mosaic structure, is determined from ω scans in which only the sample orientation is varied; the detector position, and thus the Bragg angle, remains fixed. This technique allows the individual steps of a step-graded structure, such as that in Fig. 22(a), to be resolved, as shown by the $\omega/2\theta$ scan in Fig. 22(b) [72]. The peaks in Fig. 22(b) are numbered to indicate the corresponding layer in Fig. 22(a).

A contour plot of the diffracted intensity from the relaxed Si_{1-x}Ge_x layers of the same sample is shown in Fig. 23. The Bragg angle, $\theta_B = 2\theta/2$, is plotted on the horizontal axis and the sample orientation, expressed as the difference between the position of the sample and the Bragg angle, is plotted on the vertical axis. The contours indicate the diffracted intensity on a logarithmic scale. The peaks occur at slightly negative values of $\omega - \theta_B$, indicating that the epitaxial layers are tilted slightly with respect to the substrate. This map also shows that the variation in Bragg angle for the individual layers is small compared with the variation in orientation (tilt) of the lattice planes. The large tilt variation is caused by the distortion or bending of the lattice planes by the strain fields of the dislocations.

To further test the model for the nucleation activation barrier, triple-axis measurements were made of a structure step-graded up to pure Ge having the Ge profile shown in Fig. 24 [80]. In order for relaxation to occur by the MFR mechanism, it was necessary to lower the growth temperature at higher Ge mole fraction as indicated on the figure. To determine both the alloy composition of the

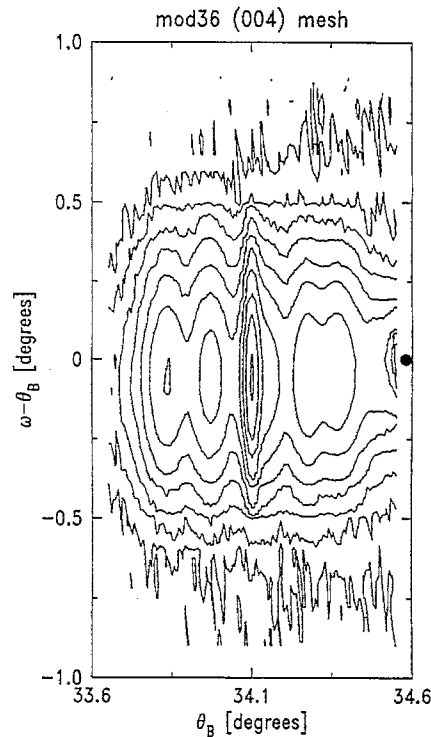


Fig. 23. Triple-axis map of the $\text{Si}_{1-x}\text{Ge}_x$ layers in the sample of Fig. 21(a) having the thicker top layer. θ_B is the Bragg angle, from which the lattice parameter is determined. ω is the angle between the sample holder and the incident X-ray beam, and indicates the sample orientation. Note that the variation in ω is much larger than the variation in θ_B , showing a large mosaic broadening caused by the dislocations. The solid circle indicates the position of the Si substrate peak.

layers and their degree of relaxation, both the symmetric 004 and asymmetric 044 reflections were measured. The steps marked with arrows on Fig. 24 were resolved in these triple-axis measurements [80]. Fig. 25 is a plot of the peak positions in reciprocal space using the coordinates Q_y and Q_z , which are inversely proportional to the in-plane and out-of-plane lattice parameters respectively [72]. The 004 data give only the out-of-plane lattice parameters, but when the 004 and 044 data are taken together, both the in-plane and out-of-plane lattice parameters can be determined. The straight line on Fig. 25 indicates equal in-plane and out-of-plane lattice parameters. The data points for all the layers fall close to this line demonstrating that all the layers are essentially fully relaxed. The alloy composition and relieved strain were calculated for each layer, as was the average tilt angle with respect to the

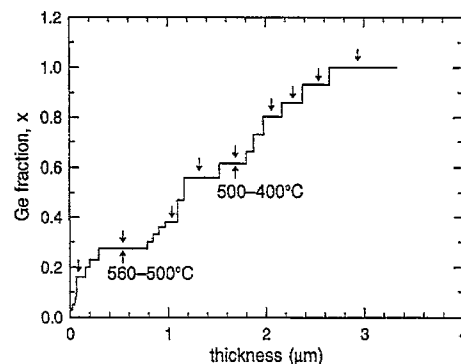


Fig. 24. Ge profile of a sample step-graded to pure Ge. (From Ref. [80].)

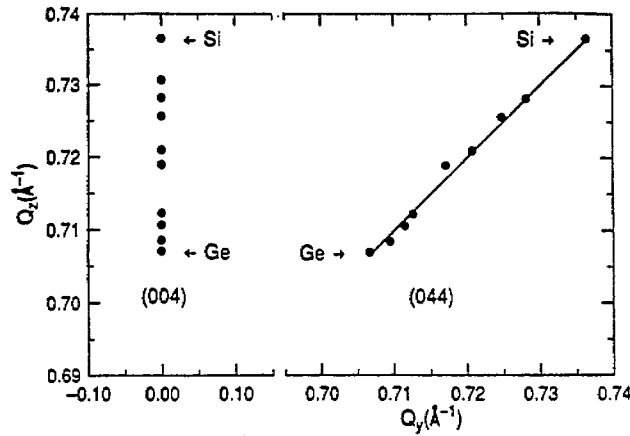


Fig. 25. Reciprocal space plot of the triple-axis X-ray diffraction peak positions of the sample of Fig. 24. Q_z is inversely proportional to the out-of-plane lattice parameter and Q_y is inversely proportional to the in-plane lattice parameter. (From Ref. [72].)

lattice planes of the substrate. These results are plotted in Fig. 26, along with the data from Fig. 20 for other UHV/CVD-grown samples. The data for the layers having $x < 0.4$ agree well with the earlier data; however, the data points for layers having $x > 0.4$ do not follow the linear relation between the tilt angle and relieved strain predicted by Eq. (3).

Eq. (2) and (3) were derived for a single layer grown on a miscut substrate at a given temperature. Although this simple model apparently works well, even for step-graded structures, when the total relieved strain is small, clearly other factors must be considered to account for the tilt angles of the higher x layers in this sample. Two modifications were made to the model [80]. First, the effect of the tilt of each relaxed step, which reduces the surface miscut for the subsequent step, was considered. When the miscut angle is reduced, the difference in the nucleation barrier on the different glide systems is also reduced and thus a smaller tilt angle is expected, as shown by the dashed curve in Fig. 26. The second modification was to include the changing materials parameters, which were assumed to vary linearly between Si and Ge, and the changing growth temperature for the different $\text{Si}_{1-x}\text{Ge}_x$ steps. The most significant parameter is the melting temperature, which is 1420 °C for Si and 937 °C for Ge. The dotted curve on Fig. 26 is expected when both these modifications are included and the data agree reasonably well, within 10%. It is clear that the varying materials parameters and growth temperature

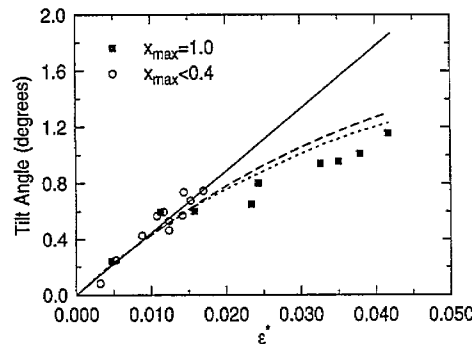


Fig. 26. Plot of the tilt angle vs. relieved strain for the sample step-graded to pure Ge (solid squares) and for lower x samples (open circles). The solid line was calculated assuming $W_n = 4.0$ eV and a constant miscut angle and ϵ_n (like Fig. 20). The dashed line was calculated taking into account the change in miscut of the surface due to the tilt of each relaxed layer. The dotted line was calculated including the changing miscut angle and also the changing materials parameters and growth temperature. (From Ref. [80].)

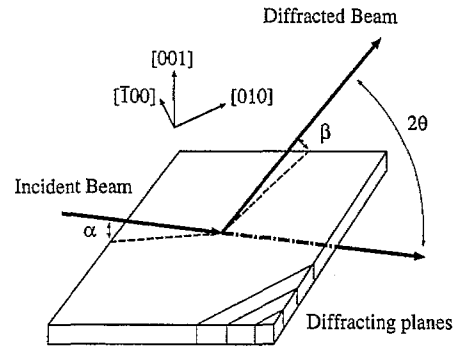


Fig. 27. Diagram showing the geometry used for grazing incidence measurements. The in-plane lattice parameter is measured directly in this geometry. (From Ref. [82].)

have a much smaller effect than accounting for the changing miscut of the growth surface. This is primarily because the lower melting temperature of the alloy at high x is offset by the lower growth temperature. Assuming that strain relaxation begins during growth of the low x layers and occurs continuously, these results suggest that a lower growth temperature is required to suppress surface roughening at higher Ge mole fraction due to the lower melting temperature.

Triple-axis X-ray diffraction measurements also allow the quantification of strain relaxation by surface roughening. A large strain variation in SiGe layers which relaxed via surface roughening was observed by both TEM and triple-axis X-ray diffraction measurements [81]. However, it is hard to obtain useful information on very thin epitaxial films in the standard geometry. Not only are the diffracted intensities very weak, but in addition the X-ray diffraction peaks are broadened when the number of atomic planes available for diffraction becomes small. To avoid this difficulty, diffraction can be done in grazing incidence geometry, in which the diffraction planes are perpendicular to the sample surface, as shown in Fig. 27 [82]. The in-plane lattice parameter is measured directly in this geometry. For convenience, scans are done in reciprocal space. H scans are equivalent to $\omega/2\theta$ scans and thus give the in-plane lattice parameter. They are plotted in units of the dimensionless reciprocal lattice unit for the silicon substrate, $H = q_x \times a_{\text{Si}}$, which for the substrate reflection is equal to -4 . K scans are essentially ω scans and thus give the range of local tilt angles. These are plotted in units of K , which for the Si substrate is equal to 0. Varying L changes the penetration depth of the X-ray beam, allowing depth profiling of the sample [82].

Fig. 28 shows H scans taken at different L values for two samples, which are similar to those in Fig. 9(c) and (d) [83]. Fig. 28(a) shows data from a very thin layer having a rough surface but no misfit dislocations. The narrow intense peak is that of the Si substrate and the very broad peak, indicating

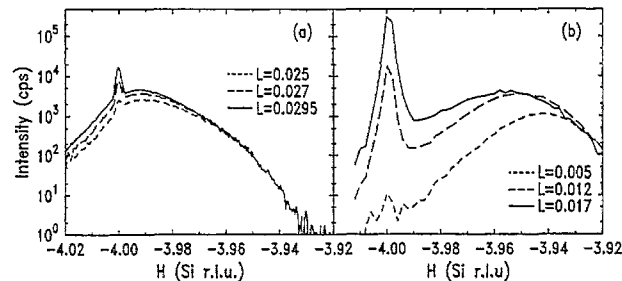


Fig. 28. H scans at different L values for the samples shown in Fig. 9 (c) and (d). The 200 Å thick layer in (a) relaxed by roughening only and the 500 Å thick layer in (b) relaxed further by the introduction of misfit dislocations. The narrow diffraction peak at $H = -4.00$ is from the Si substrate and the broad peak shows the large variation of the lattice parameter in the rough $\text{Si}_{0.7}\text{Ge}_{0.3}$ layer. (From Ref. [83].)

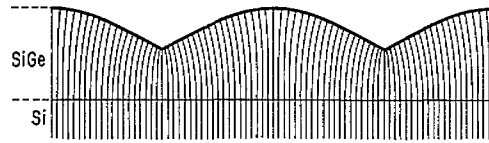


Fig. 29. Schematic diagram showing strain relaxation by surface roughening. Note the larger lattice spacing in the thicker regions of the layer and the smaller lattice spacing in the thinner parts.

a large variation in lattice parameter, is that of the epitaxial layer. On average, the in-plane lattice parameter of the SiGe layer is slightly greater than that of the substrate, indicating that surface roughening alone has indeed relieved some strain. However, the variation in lattice parameter is so great that in some regions of the layer it is smaller (the magnitude of H is larger) than that of the substrate, i.e. there are regions of very high strain, as is shown schematically in Fig. 29. Fig. 28(b) shows X-ray data for a thicker layer which has a rough surface and also misfit dislocations. At the higher values of L diffraction from both the substrate and the SiGe layer are observed, but at the lowest value of L we see only the reflection from the SiGe layer. The layer peak has shifted to $H \approx -3.94$, showing that additional strain has indeed been relieved by the dislocations. Although there is still a wide range of lattice parameters, all are greater than the lattice parameter of the substrate. Reciprocal space maps of these two samples are shown in Fig. 30. The shape of the contours shows that the variation of the lattice parameter is much greater than the variation in orientation of the lattice planes in the thinner layer, but that the dislocations have introduced additional mosaic broadening in the thicker one.

It is clear from the reciprocal space maps that dislocations in relaxed $\text{Si}_{1-x}\text{Ge}_x$ layers cause a broadening of the X-ray peaks. This broadening is primarily the result of distortions of the lattice planes by dislocation strain fields, which cause them to tilt slightly out of the (001) plane. Although misfit dislocation are primarily confined to the lower region of step-graded buffer layer structures and threading dislocation densities in the upper layers are very low, diffraction space maps such as those in Fig. 23, clearly indicate that the X-ray peaks of all the layers are broadened. Fig. 31 shows a

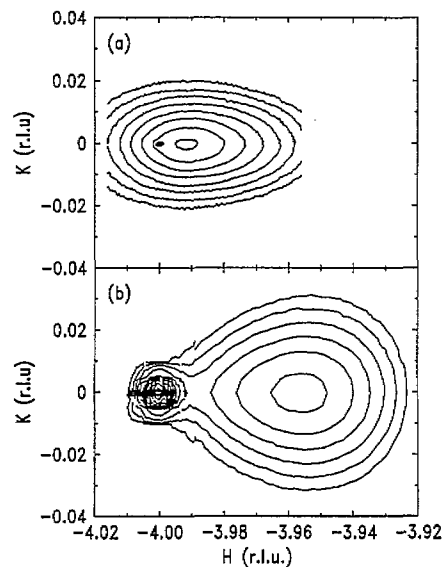


Fig. 30. Reciprocal space maps (plotted in Si reciprocal lattice units) of the two samples of Fig. 28. The narrow intense peak is diffraction from the Si substrate and the broad peak is that of the $\text{Si}_{0.7}\text{Ge}_{0.3}$ layer. Note that the sample in (b) has additional mosaic broadening owing to dislocations. (From Ref. [82].) The contours indicate the diffracted intensity on a logarithmic scale.

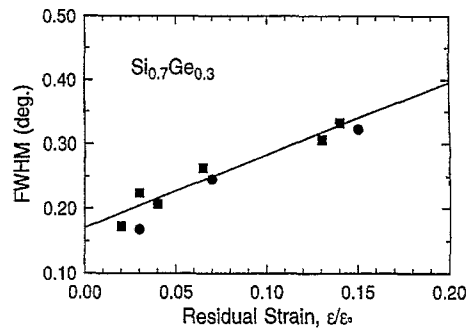


Fig. 31. Plot of the FWHM vs. residual strain of rocking curves for samples relaxed by the MFR mechanism (squares) and via surface roughening (circles).

comparison of rocking curve peak widths for two groups of samples [84]. One group of rocking curves are from the top layers of step-graded structures similar to the one in Fig. 13, which has a thick uniform composition layer on top of the step-graded region [72]. These structures relaxed by the MFR mechanism and have threading dislocation densities of about 10^7 cm^{-2} . The second group of rocking curves are from uniform composition layers, which relaxed via roughening and have threading dislocation densities of 10^{10} – 10^{12} cm^{-2} . When the same amount of strain was relieved, i.e. when the densities of misfit dislocations are equal, the X-ray peak widths are essentially equal, no matter whether the misfit dislocations are confined to a single interface or distributed in the growth direction, as is the case for the step-graded structures. The difference in peak widths between these two groups of samples, having threading dislocation densities which differed by at least three orders of magnitude, is apparently negligible, indicating that threading dislocations do not play a major role in the broadening of the X-ray peaks [84].

Others have disagreed with this conclusion [85]. From reciprocal space maps which distinguish between the top of the step-graded region and a uniform composition cap layer, they argue that the density of misfit dislocations at the interface just below the cap layer cannot account for the broadening of the X-ray peak of the cap layer, and conclude that threading dislocations in the top layer must account for this broadening. Using a model based on a random elastic deformation by the strain fields of dislocations, it was found that, although trends could be predicted, the threading dislocation density needed to account for the X-ray peak width was at least an order of magnitude larger than that determined from EBIC measurements [86]. More recent calculations of the random strains from misfit dislocations demonstrate that the major part of the broadening is caused by scattering from random strains originating from the misfit dislocations and that the contribution of the threading arms is small [87]. These calculations show that the random strains from the misfit dislocations in the lower region of the step-graded layer are not zero at the surface and thus the misfit segments account for most of the diffuse scattering. However, there is a small discrepancy between the calculation and the experiment for the upper layers of the structures where the misfit dislocation density is negligible. It was suggested that threading dislocations in these upper layers may account for this difference [87].

In this section we have discussed the use of high resolution X-ray diffraction measurements to quantify strain relaxation in $\text{Si}_{1-x}\text{Ge}_x/\text{Si}$ structures and to further study the two strain relaxation mechanisms seen in UHV/CVD-grown $\text{Si}_{1-x}\text{Ge}_x/\text{Si}(001)$ structures. A new method was developed to measure the nucleation activation barrier for dislocations, which was applied to both the MFR mechanism and nucleation via surface roughening. These results provide information useful for the design of step-graded buffer layers, which are discussed in the following section. Grazing-incidence diffraction measurements quantify the relaxation and also show the large variation in lattice parameter occurring in the case of strain relaxation via surface roughening.

3.3. Relaxed step-graded SiGe/Si buffer layers

High quality relaxed step-graded SiGe/Si buffer layers have been grown by different growth methods at temperatures ranging from about 450 to 900 °C [9,13,88]. For technological applications these structures must not only have low threading dislocation densities and flat surfaces, but must also be thermally stable at device processing temperatures, which may be higher than the growth temperature. Buffer layers grown at low temperature, in the regime where relaxation is kinetically limited, may be metastable and may therefore undergo further relaxation when subsequently heated to a higher temperature. Triple-axis X-ray diffraction was used to monitor the evolution of strain relaxation during growth and after annealing at high temperature [88,89].

Since in-situ measurements could not be made during epitaxial growth, a series of structures was prepared, each having an additional step as shown in Fig. 32 [89]. Steps having $x < 0.3$ were grown at 560 °C and those with $x \geq 0.3$ were grown at 500 °C. Samples are referred to by the number of the top layer, e.g. sample 3 has three layers, sample 4 has four layers, etc. Cross sectional TEM was used to measure the thickness of each step in each sample and to verify that relaxation occurred by the MFR mechanism. Fig. 33 shows cross sectional images of samples 3, 4 and 5. No defects are observed after the growth of layer 3, since the layer thickness is below the critical thickness for strain relaxation at this growth temperature. After the growth of layer 4, however, a low density of the dislocation pile-ups characteristic of the MFR mechanism, like the one shown in Fig. 33, were observed. Significant strain relaxation occurred during the growth of layer 5, as is seen by the higher density of dislocation pile-ups in sample 5.

Both the 004 and the 044 reflections were measured by X-ray diffraction for these samples [82,89]. Diffraction space maps of the 044 reflection are shown in Fig. 34. In this figure q_z is inversely proportional to the out-of plane lattice parameter and q_y is inversely proportional to the in-plane lattice parameter. The diffraction peaks of fully strained layers having the same in-plane lattice parameter as the Si substrate will have the same q_y coordinate as the substrate peak, and the peaks of fully relaxed layers will lie along the dashed line indicating that $q_y = q_z$. The diffraction space map of sample 3 shows two narrow peaks, those of the substrate and of layer 3. The map for sample 4 shows that the in-plane lattice parameters of layers 3 and 4 are essentially the same as that of the substrate, but the mosaic broadening of the layer peaks in the direction perpendicular to the dashed line is evidence that some dislocations are present. Although the dislocation density is not sufficient to change the in-plane lattice parameter significantly, it has a strong effect on the shapes of the SiGe layer peaks. The map of sample 5 shows that the three layers are substantially relaxed, although the peaks corresponding to layers 3 and 4 lie closer to the dashed line than does that of layer 5. There is also additional mosaic broadening owing to the increased density of misfit dislocations in this sample. The maps for the other

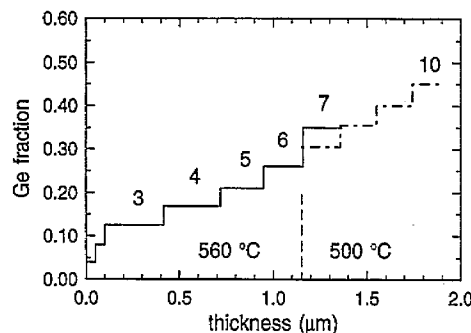


Fig. 32. Ge profile for a series of samples, each having an additional layer.

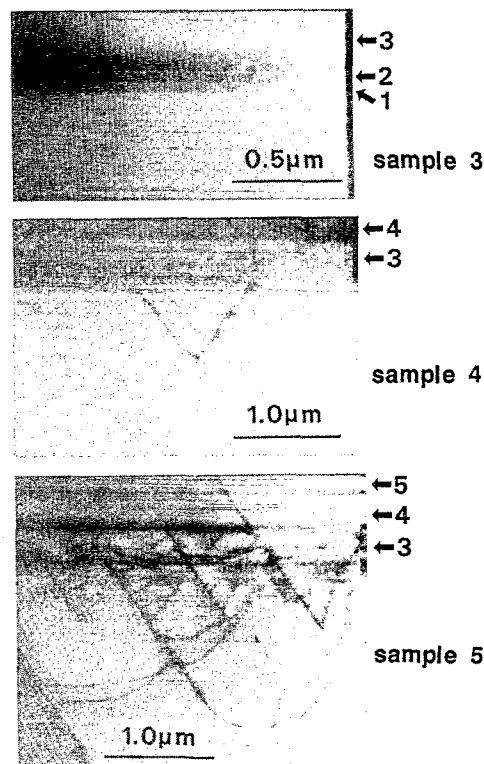


Fig. 33. Cross sectional TEM images for samples 3, 4 and 5. The layer numbers correspond to those in Fig. 32.

samples are similar to that for sample 5 and show that the top layer is less relaxed than the lower layers for this whole series.

The alloy composition and degree of relaxation of each layer was calculated from the diffraction data. From this the mismatch strain at the start of growth of each layer was determined [89] and is plotted as solid circles in Fig. 35 for samples 3 through 7. The open circles indicate the mismatch strain for two other samples. One is for an $x=0.31$ step grown on top of sample 6 (see the broken line in Fig. 32). The other is for an $x=0.50$ step on top of sample 10. This plot shows that the strain increases as layers are added to the structure until significant relaxation occurs, in this case during the growth of layer 5. When steps of equal thickness and increment in x are added, the mismatch strain at the start of growth of each step is constant. If the increment in x is increased, e.g. as in sample 7, then there is a corresponding increase in the strain. Similar results were recently reported for linearly graded buffer layers [90,91]. These measurements clearly show that after relaxation begins it occurs continuously as each new step is added to the structure such that the strain remains low. For the step structure indicated by the broken line in Fig. 32, the mismatch strain at the start of growth of the layers beginning with step 6 is equivalent to the mismatch strain of a $\text{Si}_{0.86}\text{Ge}_{0.14}$ layer grown on Si. This proves our earlier assumption that the mismatch strain is always low in step-graded structures, and confirms that the lower growth temperature required for MFR relaxation at high Ge fraction is indeed because of the lower melting temperature of the alloy.

The fact that the uppermost layer is always less relaxed than those underneath in this series of samples suggests that either the increments in Ge fraction or the step thickness should be increased to achieve a thermally stable buffer layer. Two pairs of structures having thin and thick top layers were grown having steps similar in thickness but with a slightly larger increment in the Ge mole fraction, i.e. the average Δx is 0.055 instead of 0.045. One pair is shown in Fig. 22(a) [88]. The other pair

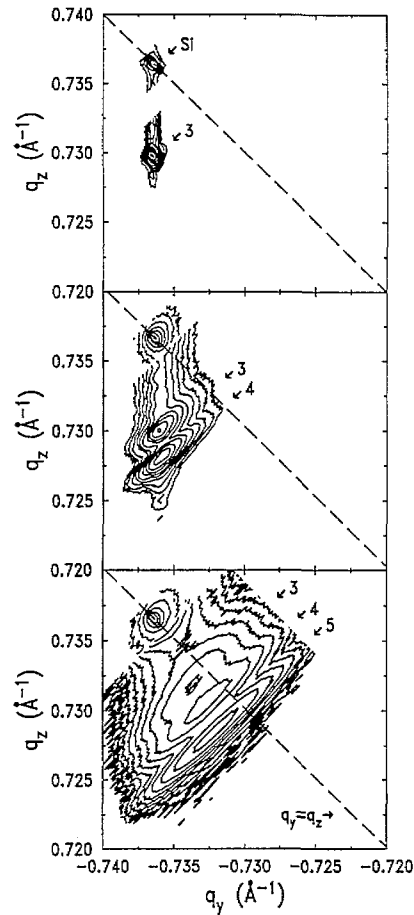


Fig. 34. Reciprocal space maps of samples 3, 4 and 5. q_z is inversely proportional to the out-of-plane lattice parameter and q_y is inversely proportional to the in-plane lattice parameter. The peak numbers correspond to the layers in Fig. 32.

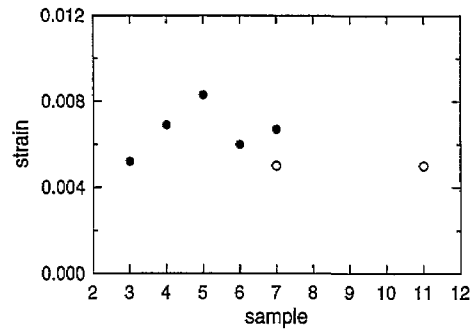


Fig. 35. Plot of the strain at the start of growth of the top layer as determined from the X-ray diffraction data. Solid circles are for those shown with a solid line in Fig. 32 and open circles are for those shown by the broken line.

was the same except that layer 5 was omitted. The X-ray measurements showed that layer 5 was too thin to have any effect on the relaxation; the two samples having thin top layers with and without layer 5 were both 90% and 91% relaxed respectively. Fig. 36 shows (004) diffraction peaks for the SiGe layers of the thin sample of Fig. 22(a) as-grown and also after annealing at 750 °C for 30 min, in an argon atmosphere. The slight shift of the peak for layer 6 is within the uncertainty of the measurement. The intensity difference is caused by a modification of the measurement set-up, not the sample.

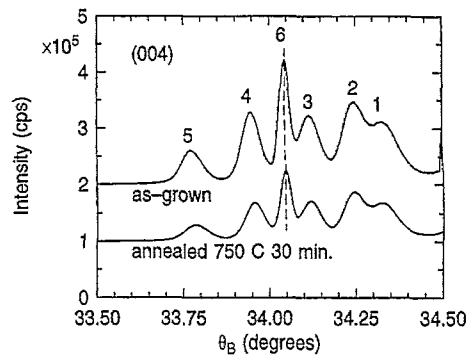


Fig. 36. X-ray diffraction from the $\text{Si}_{1-x}\text{Ge}_x$ layers of the sample in Fig. 22(a) with the thin cap layer, both as-grown and after annealing. The peak numbers correspond to the layer numbers in Fig. 22(a). (From Ref. [88].)

Although the top layer of this sample is only 90% relaxed, it is thermally stable and does not relax further upon annealing. Thus this structure is expected to withstand the thermal cycling necessary for device processing. We conclude from these results that a thickness of $1.6\ \mu\text{m}$ is sufficient to achieve a thermally stable relaxed $\text{Si}_{0.67}\text{Ge}_{0.33}$ buffer layer at these low growth temperatures. This corresponds to a grading rate of $21\% \text{ Ge } \mu\text{m}^{-1}$. When much faster grading rates were used, e.g. the structure of Fig. 13, it was necessary to grow a $1\ \mu\text{m}$ thick uniform composition layer on top of the step-graded layer to completely relieve the strain under these growth conditions [84].

Step-graded $\text{Si}_{0.68}\text{Ge}_{0.32}$ buffer layers grown by both MBE [9] and RT/CVD [66] having different grading rates have been reported. Step-graded structures grown at 820°C by RT/CVD, which did not have a $1\ \mu\text{m}$ thick uniform composition cap layer, had considerable residual strain even at grading rates lower than $20\% \text{ Ge } \mu\text{m}^{-1}$, although those having a $1\ \mu\text{m}$ thick cap layer were fully relaxed [66]. Fully relaxed buffer layer structures having grading rates up to $55\% \text{ Ge } \mu\text{m}^{-1}$ and $1\ \mu\text{m}$ thick cap layers were also achieved by MBE growth, typically in the temperature range $700\text{--}900^\circ\text{C}$ [9].

The thermal stability of buffer layer structures is very important, but the density of threading dislocations at the top of the buffer layer is also critical for device applications. Threading dislocation densities have been measured by several different techniques. Plan view TEM is useful only when the densities are high ($> 10^7 \text{ cm}^{-2}$). Both electron beam induced current (EBIC) [92] and etch pit counting are useful for measuring threading dislocation densities over a wide range [9,66]. Fig. 37 shows the surface of a sample step-graded to $\text{Si}_{0.7}\text{Ge}_{0.3}$ having a fast grading rate similar to that in Fig. 13. The upper picture shown both a scanning electron microscopy (SEM) image and an EBIC image of the surface and the lower picture is a Nomarsky image of the same sample. In addition to the cross-hatch pattern, there are rows of pits on the surface. These show up as electrically active areas on the EBIC image. These features are typical of samples with fast grading rates. Plan view TEM shows that there are bundles of threading dislocations located at the pits. Reducing the growth temperature of the uppermost layer from 560 to 500°C eliminates the pits, but not the bundles of threading dislocations. The presence of bundles indicates that there is considerable pinning of the threading segments and that therefore the annihilation process is not complete in these structures. The upper picture in Fig. 38 is an SEM image of an etched surface of a similar sample, showing that, although there are a few isolated threading dislocations, most of them occur in bundles or rows. The average density of threading dislocations in this sample is in the 10^7 cm^{-2} range.

The lower picture in Fig. 38 is an SEM image of a sample similar to those in Fig. 22(a). Using a lower grading rate has eliminated the bundles of threading dislocations and only isolated ones remain. This sample has a threading dislocation density of about 10^6 cm^{-2} . Similar results were reported for

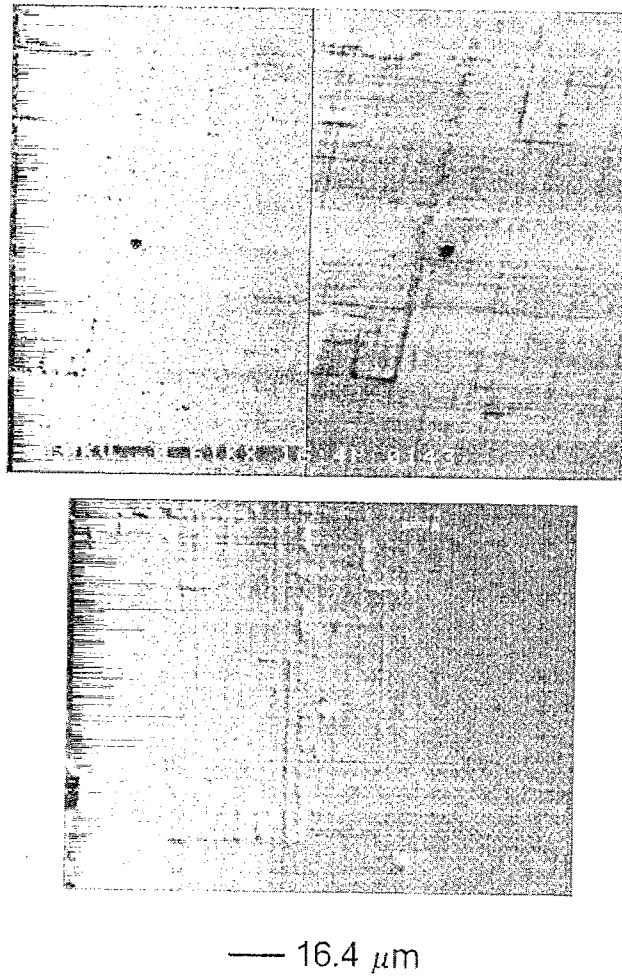


Fig. 37. The upper photograph shows SEM (left) and EBIC (right) images of a relaxed step-graded structure like that shown in Fig. 13. The lower photograph shows a Nomarsky image of the same sample. The dark contrast in the EBIC image corresponds to pits in the SEM and Nomarsky images.

MBE-grown structures step-graded to $\text{Si}_{0.68}\text{Ge}_{0.32}$, where TEM measurements show a strong dependence of the threading dislocation density on the grading rate [9]. EBIC measurements indicated a weaker dependence on grading rate, however. The different densities measured by the two techniques points out how difficult it is to get accurate measurements of threading dislocation densities, especially when they are $< 10^6 \text{ cm}^{-2}$. A strong dependence of the threading dislocation density on the grading rate, determined by etch pit counting, was reported in RT/CVD-grown structures samples, with densities as low as about 10^3 cm^{-2} when the grading rate was $3\% \text{ Ge } \mu\text{m}^{-1}$ [66]. Others report a similar variation with grading rate for RT/CVD-grown structures, but higher threading dislocation densities were measured using EBIC [66].

A lower threading dislocation density at low grading rates is expected for two reasons. First, when the grading rate is low the steps are much thicker and the misfit dislocations are spread out in the growth direction. Thus interactions between misfit segments are reduced. Second, the mismatch strain at the start of growth of each new step is lower at lower grading rates, as seen by the data for the two different versions of sample 7 in Fig. 35, and therefore the average value of the strain at which dislocation occurs is lower. It is clear from Fig. 21 that it is preferable for dislocation nucleation to occur at low mismatch strain.

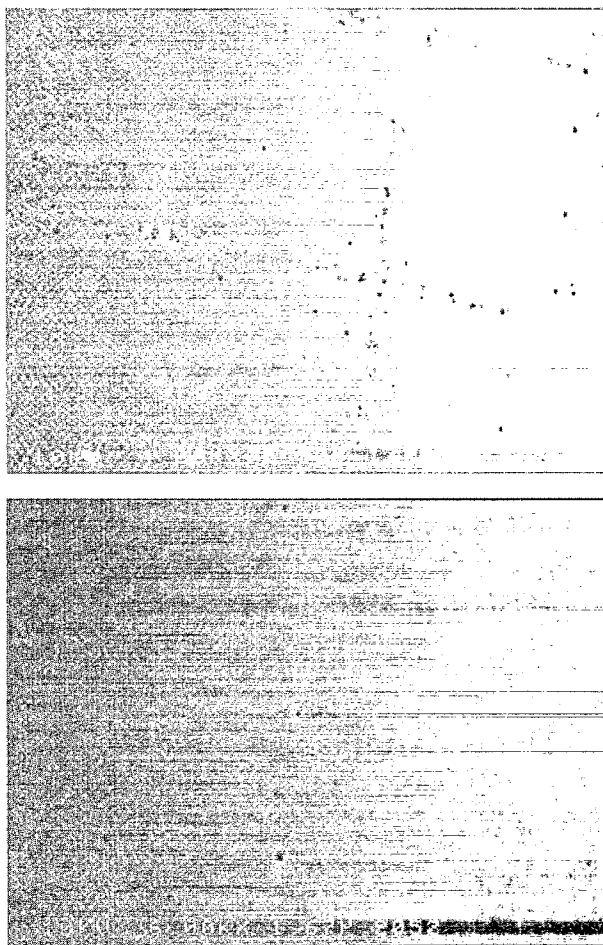


Fig. 38. SEM images showing etch pits in step-graded structures having a fast grading rate like that in Fig. 13 (upper) and a slower grading rate like that in Fig. 22(a) (lower). The upper image shows bundles and rows of threading dislocations like the images in Fig. 37, while the lower image shows only individual threading dislocations.

Surface roughness is also an issue, if the buffer layers are to be used for devices requiring fine-line photolithography. AFM measurements on UHV/CVD-grown layers such as those in Fig. 22(a) show that the root-mean-squared (RMS) amplitude of the cross-hatch pattern is $< 60 \text{ \AA}$ [88]. The RMS amplitude of the cross hatch pattern was smaller at lower grading rates in RT/CVD-grown buffer layers, and was $< 100 \text{ \AA}$ when grading rates were $< 30\% \text{ Ge } \mu\text{m}^{-1}$ [66]. For a grading rate of $10\% \text{ Ge } \mu\text{m}^{-1}$, the RMS amplitude of the cross-hatch pattern was found to increase monotonically with the Ge mole fraction of the top layer, but was $< 100 \text{ \AA}$ up to $x \approx 0.8$ [93]. Thus it does not appear that surface roughness will cause problems for photolithography. As will be discussed in the following section, the effects of interface roughness on electronic properties are determined by the lateral spacing of the surface features as well as the amplitude of the roughness in the growth direction.

Another important consideration is the lateral uniformity of these relaxed buffer layers, if they are to be useful technological applications. In order for a relaxed layer to have a uniform in-plane lattice parameter, not only must the alloy composition of the various layers be uniform, but also the strain as well. Cross sectional TEM images show dislocation pile-ups, suggesting that there must be some variation in the strain across the surface. The lateral and vertical uniformity of layers like the one in Fig. 13 was investigated using Raman scattering [94]. Like X-ray diffraction, Raman scattering

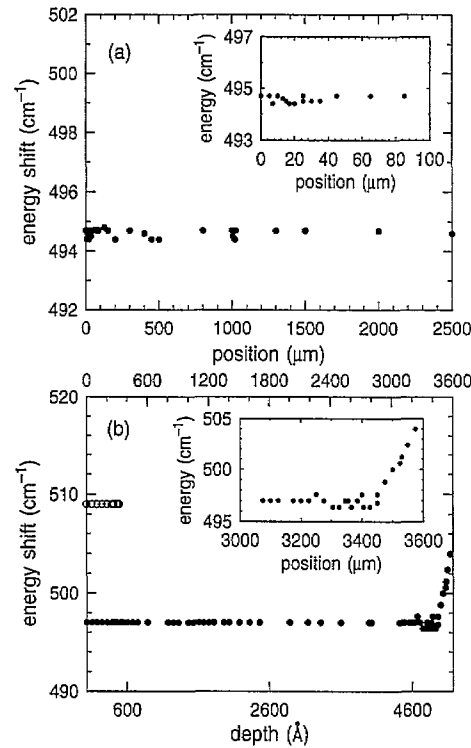


Fig. 39. Plot of the energy shift of the Si-Si phonon vs. the position of the sample. The insets show expanded regions of each plot: (a) only the lateral position is varied, and (b) the sample was beveled so that the change in lateral position corresponds to a change in depth. (From Ref. [94].)

can be used to determine the composition and strain in a $\text{Si}_{1-x}\text{Ge}_x$ film, using the energy position and relative amplitudes of the Si-Si, Ge-Ge and Si-Ge vibrational modes [95]. One advantage of Raman scattering is that the size of the probe is only about $1\text{ }\mu\text{m}$, compared with $1\text{--}10\text{ mm}$ for X-ray diffraction, depending on the X-ray source used. A disadvantage is that Raman scattering is much less sensitive to differences in strain than X-ray diffraction. Nevertheless, Raman scattering measurements can give an upper limit on the strain variations in these layers.

Measurements of the lateral uniformity of these structures were made by moving the sample under the laser beam over distances of several millimeters. A sample polished at an angle of 2 min with respect to the original surface, thus combining a variation in depth with lateral movement, was also measured. The samples measured have Ge profiles similar to the one in Fig. 13, i.e. they have relatively fast grading rates. Fig. 39 shows the energy position of the Si-Si mode at different positions of the sample [94]. As is clearly seen, the variation in energy for both samples is $< 1\text{ cm}^{-1}$, i.e. it is within the uncertainty of the measurement. For $\text{Si}_{0.7}\text{Ge}_{0.3}$ this corresponds to compositional fluctuations of $x < \pm 0.01$ or residual strain variations of about $\pm 5\%$ of the total mismatch strain [94]. Apparently the misfit dislocations are sufficiently far from the sample surface that the strain field at the surface is uniform on a lateral scale of microns and it is uniform on a lateral scale of several millimeters as well. If the alloy composition varies only by $x = \pm 0.01$ over the whole wafer (and we know from measurements of devices fabricated with strained layers grown in the same reactor that the variation is negligible), a strain variation of about $\pm 5\%$ is expected over the entire wafer as well.

It has been shown that from a structural perspective that step-graded relaxed SiGe/Si buffer layers have characteristics suitable for the applications discussed in Section 2. They can be grown by a variety of techniques, including some which are suitable for use in manufacturing. $\text{Si}_{0.7}\text{Ge}_{0.3}$ buffer

layer structures have been shown to be thermally stable and, despite the cross-hatch pattern, the surface roughness is within acceptable limits. Reasonably low threading dislocation densities, in some case as low as 10^3 cm^{-2} but more typically in the 10^5 cm^{-2} range, have also been reported by a number of different groups using different growth methods. The maximum threading dislocation densities tolerable for various applications have not yet been definitively established. Threading dislocations are expected to affect the performance of individual devices and their density will thus determine which devices structures are possible and the ultimate levels of device integration which can be achieved. In the following sections we will examine the effects of surface/interface roughness and dislocations on the electronic and optical properties of the buffer layers and on device layers grown on them.

4. Effects of dislocations on the electronic properties of relaxed SiGe structures

The presence of dislocations in relaxed SiGe Buffer layers can affect the properties of these films in at least two different ways. As was already discussed, the strain field of the dislocation distorts the atomic planes in the crystal, leading to broad X-ray diffraction peaks. Dislocation strain fields, which extend over a much larger volume of space than the dislocation core, can also scatter electrons, thus reducing the low temperature electron mobility [21,25,27,29]. Similarly strain variations introduced by interface roughening can reduce electron mobility at low temperature [28,29]. There may also be localized electronic states associated with dislocations. These may be intrinsic states of the dislocation core or may involve point defects such as impurity atoms or Si or Ge vacancies or interstitials or complexes of point defects. These localized states may act as radiative or non-radiative recombination centers, thus reducing band gap photoluminescence, or they may act as hole or electron traps, which can compensate shallow dopant impurities. If present in significant concentrations, localized states can change carrier lifetimes and cause leakage currents or threshold shifts in devices. Some device processing steps may also be effected by the presence of dislocations in these relaxed structures, e.g. impurity diffusion or gettering at threading dislocations during annealing following ion implantation or during processes such as reactive ion etching.

In the following sections we discuss the effects of strain variations due to dislocations and to rough interfaces on low temperature electron mobility. We also review work on recombination and trapping at localized electronic states in relaxed $\text{Si}_{1-x}\text{Ge}_x$ layers. Device processing problems owing to dislocations are not discussed here, as these have not yet been extensively investigated. We note that such problems have apparently not been a serious limitation for the devices reported so far. It is clear from the high values achieved for the low temperature electron mobility that, while strain variations do effect electron scattering at low temperature, proper design of the layer structure can minimize the effects of these scattering sources. The concentrations of localized states in step-graded buffer layers are sufficiently low that significant negative effects are not expected.

4.1. *Effects of strain fields on low temperature electron mobility*

There is no evidence that distortions of the lattice planes leading to mosaic broadening of the X-ray diffraction peaks, but not to large variation in the lattice parameter, of step-graded buffer layers affect the electronic properties of relaxed SiGe/Si structures. However, it has been shown that variations in strain owing to interface roughness provide a scattering source which can affect the low temperature electron mobility [28,29]. Three components were found in the Fourier spectra of the surface roughness of relaxed step-graded $\text{Si}_{1-x}\text{Ge}_x/\text{Si}$ structures measured by AFM [28]. One component corresponds to atomic scale roughness, one to roughness similar to that in Fig. 11(a) and one to the cross-hatch

pattern shown in Fig. 11(b). The correlation length of the roughness component corresponding to the cross hatch pattern is $\sim 1 \mu\text{m}$. Integrated circuits currently have features comparable with or smaller than this length. Therefore minimizing this roughness component is important for lithographically defined process steps such as metal deposition. As discussed in Section 3.3, RMS amplitudes of $< 100 \text{ \AA}$ have been achieved with various growth techniques for $\text{Si}_{0.7}\text{Ge}_{0.3}$ buffer layers.

The roughness component corresponding to island growth (Fig. 11(a)), which has a correlation length of $\sim 300 \text{ \AA}$, affects the low temperature electron mobility, when it occurs at the upper interface of the Si channel where the two-dimensional electron gas (2DEG) is located (see Fig. 2) [28]. Strain variations caused by this roughness component, as indicated by the large variation in lattice parameter shown in Figs. 28-30, were demonstrated to be a source of electron scattering which, in this highly strained system, is significantly larger than conventional geometric roughness scattering [29]. As discussed in Section 3.1, this component of the surface or interface roughness is driven by mismatch strain and occurs when the growth temperature is sufficiently large relative to the melting temperature of the material that surface atoms are mobile. This roughness component can occur for layers under either tensile or compressive strain, but a marked increase in the roughness amplitude is observed for layers under compressive strain larger than $\sim 1.4\%$ [96]. Roughening is suppressed at lower mismatch strain in UHV/CVD-grown material by reducing the growth temperature.

Dislocation strain fields also provide a source of electron scattering at low temperature [21,25,27,29]. A series of systematic experiments was done to investigate the effects of threading dislocations passing through the Si channel, the effects of misfit dislocations at the interface between the relaxed $\text{Si}_{1-x}\text{Ge}_x$ buffer layer and the bottom of the Si channel, and the effects of misfit dislocations in the lower part of the step-graded $\text{Si}_{1-x}\text{Ge}_x$ buffer layer [25]. Varying the grading rate of the relaxed buffer yielded samples with threading dislocation densities ranging from 10^5 to 10^{11} cm^{-2} . The low temperature electron mobility was found to be sensitive to threading dislocations when their density exceeds $3 \times 10^8 \text{ cm}^{-2}$, and it decreases by two orders of magnitude when the density is $1 \times 10^{11} \text{ cm}^{-2}$. To evaluate the effects of misfit dislocations in the step-graded buffer layer, uniform composition layers of varying thickness were grown between the top of the step-graded buffer and the Si channel. The low temperature electron mobility increased strongly when the thickness of the uniform layer was increased up to about $0.5 \mu\text{m}$; beyond this thickness the increases in mobility were very small. This result is consistent with estimates of the range of variations in the strain field of dislocations in the step-graded buffer layer [9,27].

Finally, the thickness of the strained Si channel was varied to evaluate the effects of misfit dislocations at the lower interface of the Si channel [21,25]. As shown schematically in Fig. 6(a), when the thickness of the Si channel exceeds the Matthews–Blakesley critical thickness, threading dislocations at the top of the step-graded buffer layer glide in the Si channel during growth to form misfit dislocations at the interface at the bottom of the channel (labeled “interface of interest” in Fig. 2). The low temperature electron mobility was measured as a function of the channel thickness and was found to decrease just at the critical thickness for dislocation glide. Plan view TEM images show the presence of long misfit segments at the interface, and the low temperature electron mobility decreases rapidly as the density of the misfit segments increases. Electron scattering by the strain fields of these misfit dislocations was calculated, assuming that the dislocation spacing is large compared with the electron wavelength [29]. The calculated mobility drops dramatically with the onset of misfit dislocation formation, with the mobility inversely proportional to the dislocation density, in reasonable agreement with the experimental results of Refs. [21] and [25]. The scattering by dislocation strain fields can be eliminated in properly designed structures. In any case, this scattering mechanism is not important at room temperature.

4.2. Localized electronic states in relaxed $\text{Si}_{1-x}\text{Ge}_x$ layers

Defects or impurity energy levels which lie in the forbidden energy gap can affect the optical and electronic properties of the material and defects having such states are said to be electrically or optically active. The observation of EBIC images of bundles of threading dislocations (e.g. Fig. 37) or of individual threading dislocations [9] suggests that threading dislocations are electrically active. Measurements of the surface photovoltage also suggest that threading dislocations are electrically active. The photovoltage induced by the scanning tip of a near-field optical microscope (NSOM) was correlated with the surface morphology of MBE-grown step-graded SiGe buffer layers [97]. A small pit, about 100 Å deep and about 0.4 μm in diameter is seen in the topographic image. A somewhat larger pit, about 0.7 μm in diameter, corresponding to a 10% reduction in the photovoltage, is seen in the corresponding photovoltage image. Features in EBIC images of the same samples are about 1 μm in diameter. The electrical images are both larger than the topographic image because the length scale for the electrical activity is determined by carrier diffusion as well as the size of the excitation beam. Observation of these features in both the photovoltage and EBIC images indicates that they act as recombination centers. It is believed that these features correspond to individual threading dislocations both because of the size of the features and because both the magnitude of the contrast and spatial extent of these features vary little from defect to defect. Further evidence that dislocations in relaxed $\text{Si}_{1-x}\text{Ge}_x$ are electrically active comes from simultaneous measurements of the I - V curves and structural characteristics of a p-n junction structure using TEM [98]. Specimens were heated in-situ to induce relaxation and a linear relation was found between the reverse bias current of the device and the misfit dislocation density.

Calculations of the electronic structure of both 30° and 90° partial dislocations in Si indicate that a reconstruction of the dislocation core is energetically favored, analogous to that which occurs at a Si surface [99,100]. The atoms move slightly to allow the dangling bonds to pair up, and thus no deep levels are expected in the case of perfect reconstruction. However, reconstruction defects can occur when the pairing is not perfect and a single dangling bond results [101]. These are called anti-phase defects (APDs). In the SiGe/Si(001) structures of interest here, dislocation motion occurs by glide. As pointed out in Section 3, the data in these structures support the model that glide occurs by the formation and motion of double kinks. Recent theoretical work has focussed on calculating the energies for kink formation and kink motion in Si [101–104]. These calculations show that kinks in both the 30° and the 90° partial dislocations have energy levels in the forbidden gap. Thus kink states and APDs are intrinsic states of the dislocation core which one might expect to find in relaxed $\text{Si}_{1-x}\text{Ge}_x$ buffer layers.

It is known from studies of plastically deformed Si that localized electronic states are associated with dislocations. These states were investigated using low temperature photoluminescence (PL) and deep level transient spectroscopy (DLTS). PL and DLTS measurements performed on relaxed SiGe layers are reviewed here. Results are interpreted by comparison with theoretical and experimental work in plastically deformed or laser annealed Si. However, such comparisons must be done with caution since dislocation motion during plastic deformation can occur by processes such as climb or mixed climb and glide, which are not observed during relaxation of epitaxial $\text{Si}_{1-x}\text{Ge}_x$ layers at low mismatch strain.

Fig. 40 shows PL spectra for relaxed UHV/CVD-grown $\text{Si}_{1-x}\text{Ge}_x$ /Si structures like that shown in Fig. 13 [105]. Three undoped samples have uniform composition $\text{Si}_{1-x}\text{Ge}_x$ cap layers having $x = 0.30, 0.29$ or 0.15 ; a fourth sample is boron-doped with a cap layer having $x = 0.32$. Starting from the high end of the spectrum, we observe the transverse optical (TO) phonon replica of the bound exciton originating from the Si substrate, denoted by Si:BE_{TO} . At slightly lower energies we observe

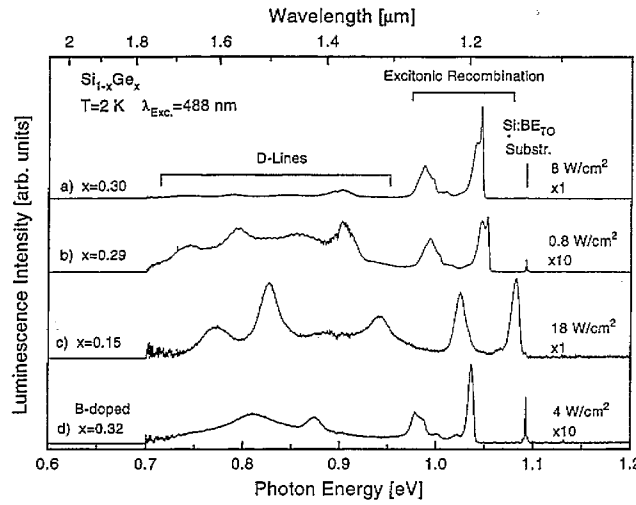


Fig. 40. PL data for the cap layers of four relaxed step-graded $\text{Si}_{1-x}\text{Ge}_x$ structures similar to that in Fig. 13. Recombination at the band-edge and at dislocations is observed. Note the peak shift of the $x=0.15$ sample corresponding to the different band gap. (From Ref. [105].)

the band-gap luminescence consisting of no-phonon bound exciton lines, $\text{BE}(x)^{\text{NP}}$; excitons are bound at alloy fluctuations or impurities, depending on the sample and the measurement conditions. Phonon replicas of these lines are seen as transverse acoustical (TA) or TO phonons in the Si-Si, Si-Ge or Ge-Ge modes [106]. Note that these lines are shifted to higher energy in the $x=0.15$ sample compared with the $x=0.3$ samples owing to the larger band gap energy. At lower energies luminescence features originating from dislocations, the D lines whose energy position also varies with the alloy composition, can be seen [107,108]. The observation of near band-gap PL clearly demonstrates that competing recombination processes, both radiative and non-radiative, have a minimal effect in these samples.

Varying the measurement temperature and the excitation power reveals that the near band-edge luminescence consists of three different recombination processes as shown in Fig. 41 [105]. These include recombination of excitons bound to alloy fluctuations, $\text{BE}(\text{af})^{\text{NP}}$, and excitons bound to shallow

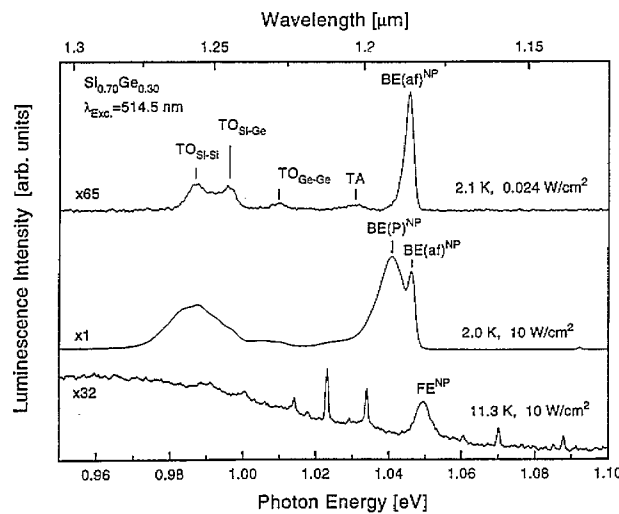


Fig. 41. Band-edge recombination at different excitation power and measurements temperature in a relaxed SiGe layer. Excitons bound to alloy fluctuations, $\text{BE}(\text{af})^{\text{NP}}$, excitons bound to shallow impurities, $\text{BE}(\text{P})^{\text{NP}}$, and free excitons, FE^{NP} , are observed, as are phonon replicas of the bound excitons. (From Ref. [105].)

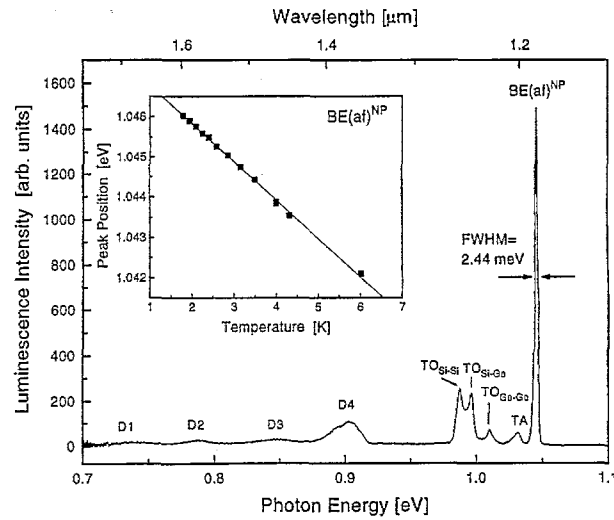


Fig. 42. Spectrum of the same sample as Fig. 41 but with excitation wavelength 458 nm. Note that the spectrum is the same but the lines are slightly narrower. The four D lines are clearly indicated on this spectrum. The insert shows variation with temperature of the energy position of the $\text{BE(af)}^{\text{NP}}$ line. (From Ref. [105].)

impurities, in this case phosphorous, BE(P)^{NP} . The third process, seen at higher temperature and high exciton power, is recombination of a free exciton, FE^{NP} . Similar spectral features have been reported for bulk $\text{Si}_{1-x}\text{Ge}_x$ crystals [109] and are also observed in strained SiGe quantum wells [110–113]. These features, along with the four D lines at lower energy owing to recombination at dislocation states, are more clearly defined when the excitation wavelength is lower, as seen in Fig. 42 [105]. The very narrow width of the $\text{BE(af)}^{\text{NP}}$, 2.44 eV, compares favorably with values of 5 meV reported for material grown by liquid phase epitaxy [114]. The slightly broader linewidth compared to 1.6 meV reported for bulk $\text{Si}_{1-x}\text{Ge}_x$ [109] may be owing to inhomogeneities in residual strain. As expected, only the exciton bound to the shallow impurity, in this case boron, is seen in the boron-doped sample. Linewidths for impurity bound exciton recombination are 6–8 meV, comparable with those found in bulk $\text{Si}_{1-x}\text{Ge}_x$ layers.

Both band-edge recombination and the D lines were also observed in spectra of relaxed step-graded buffer layer structures grown by MBE [115,116], and also in relaxed layers grown by RT/CVD [112,117] and by AP/CVD [118]. In AP/CVD samples, the intensities of both the D_3 and D_4 lines were correlated with the density of threading dislocations, as measured by etch pit counting [118]. The D_1 and D_2 lines were found to be more intense in regions of the samples with dense misfit dislocation networks. In MBE samples [115,116], the D_1 and D_2 lines were weak in the uniform composition cap layer, which has a low density of threading dislocations, but were two orders of magnitude more intense in the graded region having a high density of misfit dislocations. In contrast, the D_4 intensity was constant in both the cap layer and the step-graded region. Broad luminescence features, whose origin has not been determined, were also sometimes observed in relaxed $\text{Si}_{1-x}\text{Ge}_x$ layers [115,117,118].

Although the D lines are clearly linked with dislocations, their microscopic origin has been somewhat controversial. The question is whether recombination occurs at intrinsic dislocation states such as dangling bonds at the dislocation core, at impurity-related states located at or near the dislocation core, or at isolated point defects in the strain field of the dislocation. Various experiments have been performed in order to distinguish between these types of defect states.

PL measurements of high purity Si samples, which were plastically deformed at 650 °C, show the narrow peaks of the four D lines having roughly equal intensities at low dislocation densities

[110]. When the dislocation density is increased, these lines broaden and overlap. However, after annealing a heavily dislocated sample at 850 °C for 30 min, the narrow D lines are again observed but the D₃ and D₄ lines are in this case an order of magnitude less intense than the D₁ and D₂ lines. Studies of samples in which dislocations were introduced in different ways and which were heat treated under different conditions lead to the conclusion that the D₃ and D₄ lines are more characteristic of the dislocations themselves than the D₁ and D₂ lines.

Similar conclusions were reached from other experiments on plastically deformed high purity Si, in this case deformed at 750 °C [119]. The four D lines were very weak or not observed at all after deformation and no EBIC contrast was observed. After deliberate surface contamination with different metals and annealing at 900 °C, however, the intensities of the D lines, especially D₁ and D₂, had increased dramatically and EBIC contrast was also observed. At very high levels of metal contamination the intensities of the D lines decreased and disappeared. At high levels of contamination precipitates were observed at the dislocations by TEM. EBIC contrast was observed at all levels of contamination. Cathodoluminescence (CL) measurements, in which luminescence is spatially resolved, showed that the D₃ and D₄ are more closely related to the dislocation core than D₁ and D₂. Quenching of the D lines by metal contamination was also observed in another experiment on samples in which dislocations were induced by laser heating of the Si wafer [109]. It was suggested that D₁ is a phonon replica of D₂ and D₃ is a phonon replica of D₄, and that the D₁ and D₂ lines originate at the stacking fault between the two partial dislocations. The D lines are seen in samples where dislocations were introduced by different methods or during epitaxial growth at different temperatures and it is therefore clear that these are owing to recombination at dislocations. However, the microscopic nature of these recombination centers is still controversial.

DLTS measurements of localized states in relaxed SiGe layers have also been reported. The first report was on CVD-grown samples with low Ge mole fraction, i.e. $x < 0.15$ [120]. The trap common to all these intentionally undoped layers has an energy level near mid-gap at $E_c - 0.5$ eV. Measurements of RT/CVD layers grown at 800 °C show the presence of both electron and hole traps [112,121,122]. Hole traps with energy levels at $E_v + 0.51$ eV and $E_v + 0.38$ eV have been associated with misfit dislocations at the SiGe/Si interface and their threading arms in the SiGe layer respectively [121]. Comparison with measurements of deep states in plastically deformed Si suggest that an electron trap at $E_c - 0.6$ eV could be a state of the dislocation core, whereas the hole traps are attributed to either dislocation core states or Cottrell atmospheres, i.e. point defects trapped in the strain fields of the dislocations [112,122]. From another experiment [123], however, it was suggested that levels at $E_c - 0.24$ eV and $E_c - 0.59$ eV are associated with intentional Cu contamination and a level at $E_c - 0.32$ eV is dislocation related. After exposure to hydrogen the DLTS peaks were passivated but the D lines were not, indicating that there is no correlation between the DLTS peaks and the D lines.

A DLTS study of plastically deformed n- and p-type Si showed the presence of numerous different electron and hole traps [124,125]. The spectra of both n- and p-type samples are dominated by a trap having a level at $E_c = 0.68$ eV, which is a very efficient recombination center. The concentrations of most traps are reduced after annealing for 1 h at 700, 800 or 900 °C. The only trap remaining after the last anneal was an electron trap at $E_c = 0.38$ eV. It was concluded that this level is associated with the dislocation core and it was suggested that this electron trap may be associated with a dislocation kink. The other traps, which anneal out, were thought to arise from point defect complexes which are produced by nonconservative jog motion of dislocations during the deformation process. As pointed out earlier, such defect motion is not expected in the Si_{1-x}Ge_x/Si structures under discussion here.

DLTS measurements have also been made on MBE-grown Si_{1-x}Ge_x/Si samples [126,127]. In one case a number of traps were found but it was concluded that the traps observed were very likely related to Fe contamination in the film [126]. In another case, three hole traps were found in Si_{0.86}Ge_{0.14}

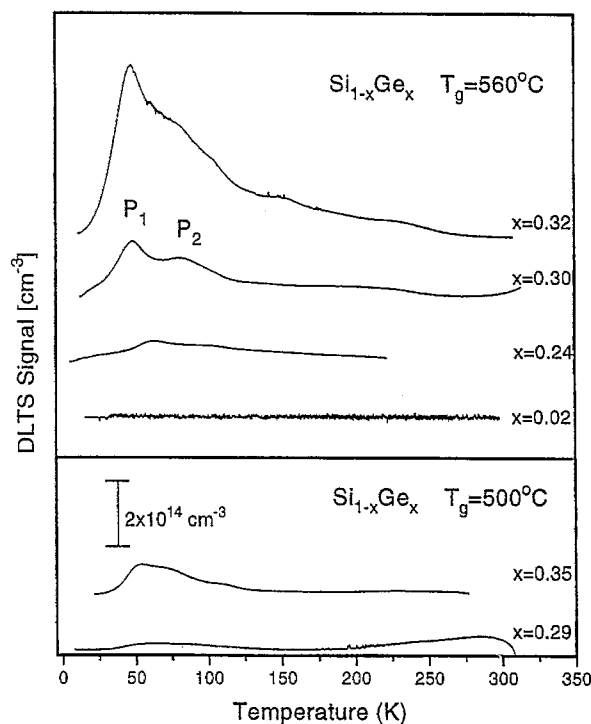


Fig. 43. DLTS spectra for a series of samples similar to that in Fig. 13. The dominant peaks, labeled P_1 and P_2 are hole traps lying close to the valence band edge. Note that the trap concentrations

at $E_v + 0.03$ eV, $E_v + 0.06$ eV and at $E_v + 0.32$ eV [127]. These were not conclusively identified, but were not attributed to dislocations. The energy levels were found to move deeper into the gap as the Ge mole fraction of the SiGe layer was increased; the two deeper levels are at $E_v + 0.26$ eV and $E_v + 0.45$ eV in $\text{Si}_{0.74}\text{Ge}_{0.26}$.

Fig. 43 shows DLTS spectra taken in one-sided abrupt p-n junctions with depletion regions at the top of the uniform composition layer of relaxed step-graded structures grown by UHV/CVD, similar to the one in Fig. 13 [128]. The two dominant traps in B-doped layers, labeled P_1 and P_2 on Fig. 43 were also observed as minority carrier traps in a P-doped layer, suggesting that neither dopant is a constituent. No electron traps were observed in any of these samples. Trap concentrations in the higher temperature range of the DLTS spectra were very low compared with these two traps. Therefore, these relatively shallow levels could determine the conductivity of undoped buffer layers. The energy levels of P_1 and P_2 are $E_v + 0.06$ eV and $E_v + 0.14$ eV in samples with $0.3 < x < 0.35$. When $x = 0.24$, the levels are $E_v + 0.09$ eV and $E_v + 0.19$ eV. These levels move closer to the valence band as x is increased, unlike the traps in MBE-grown samples. The capture behavior of these traps indicates that there is negligible lattice relaxation associated with charge capture and emission. The variation of the DLTS peak amplitude has been shown to increase logarithmically with the filling pulse duration for a deep level associated with an extended defect, whereas it increases exponentially for an isolated point defect [129]. A logarithmic relation was observed for both P_1 and P_2 , indicating that these traps are associated with extended defects, not isolated point defects.

The threading dislocation densities in these relaxed layers increased as the Ge mole fraction, and thus the relieved strain, increased. Owing to the fast grading rate, threading dislocation densities were in the 10^7 cm^{-2} range when the composition of the cap layer was $\text{Si}_{0.7}\text{Ge}_{0.3}$. The concentrations of P_1 and P_2 increased monotonically with increasing threading dislocation density in samples grown at a

given temperature, as shown in Fig. 43. However, when the growth temperature of the cap layer was reduced, a decrease in the trap concentration was observed, although there was no corresponding decrease in the threading dislocation density. The trap concentrations correlate with the oxygen concentration in the cap layer, suggesting that the defect involves oxygen at the threading dislocation. Preliminary annealing data show that these traps start to anneal out at about 700 °C, consistent with the fact that these traps are not observed in relaxed SiGe layers grown at higher temperatures. From the available annealing data there appears to be no correlation between the P_1 and P_2 traps and the D lines. This is reasonable, since one would not expect levels lying close to the band edge to be effective recombination centers.

It is clear from the DLTS measurements described above that different electron and hole traps are observed in relaxed $\text{Si}_{1-x}\text{Ge}_x$ layers, depending on the growth method and growth temperature. In contrast, the same PL lines are observed in samples containing dislocations, no matter which growth method was used for relaxed epitaxial $\text{Si}_{1-x}\text{Ge}_x$ layers or if the dislocation were introduced in bulk silicon by plastic deformation. This suggests that a correlation between the PL lines and the DLTS peaks should not be expected. It also suggests that the DLTS measurements are more sensitive to variations in background impurities or to defect complexes than are PL measurements. Further systematic work is clearly needed to understand the origin of both the D lines in the PL spectra and the various electron and hole traps in the DLTS spectra of relaxed $\text{Si}_{1-x}\text{Ge}_x$ layers. Nevertheless, both these measurement techniques are useful for monitoring the quality of relaxed SiGe layers and for optimizing the growth conditions and the design of the buffer layer structures. The trap concentrations in step-graded SiGe buffer layer structures measured by DLTS are consistent with the background doping densities, $< 10^{15} \text{ cm}^{-3}$, inferred from the high values of the low temperature electron mobility.

5. Conclusions

High quality relaxed SiGe/Si buffer layer structures have been grown epitaxially by several different growth methods. The extraordinarily high values of electron mobility at low temperature achieved in Si quantum wells grown on these buffer layers is a measure of their quality and also demonstrates that the many parameters required for complex device structures can be reproducibly controlled using these growth methods. Several important technological applications utilizing step-graded relaxed SiGe/Si buffer layers, including SiGe CMOS device, have been proposed.

Strain relaxation in SiGe/Si(001) has received a great deal of attention in recent years. Dislocation glide is well understood and several mechanisms for dislocation nucleation have been extensively studied as well. Much less well understood are the effects of dislocations on the electronic properties of relaxed $\text{Si}_{1-x}\text{Ge}_x$ layers. PL spectra of a wide variety of samples show similar features. On the contrary, the electronic states observed by DLTS vary with the growth conditions, especially the growth temperature, of the samples. The microscopic origin of these electronic states and also the recombination centers observed by PL remains controversial.

Acknowledgements

I would like to thank the many colleagues with whom I have worked on problems related to relaxed SiGe/Si buffer layer structures during the last five years. I have learned much from all of them and have enjoyed these collaborations enormously. This work has had the strong support of several different IBM managers during this period; their advice and encouragement is also greatly appreciated.

References

- [1] R.L. Gunshor and A.V. Nurmikko, *MRS Bulletin*, 20 (7) (1995) 17; S. Guha, *Semicond. Sci. Technol.*, in press.
- [2] S.L. Yellen, A.H. Shepard, R.J. Dalby, J.A. Baumann, H.B. Serreze, T.S. Guido, R. Soltz, K.J. Bystrom, C.M. Harding and R.G. Waters, *IEEE J. Quantum Electron.*, 29 (1993) 2058.
- [3] P.J. Tasker, in D.V. Morgan and R.H. Williams (eds.), *Physics and Technology of heterojunction Devices*, Ch. 5, Peter Peregrinus Ltd, London, 1991.
- [4] B.S. Meyerson, D.L. Harnage, J. Stork, E. Crabbe, J. Comfort and G. Patton, *Int. J. High Speed Electron. Systems*, 5 (1994) 473.
- [5] K. Ismail, S. Rishton, J.O. Chu, K. Chan, S.F. Nelson and B.S. Meyerson, *IEEE Electron Device Lett.*, EDL-14 (1993) 348.
- [6] M. Arafa, P. Fay, K. Ismail, J.O. Chu, B.S. Meyerson and I. Adesida, *IEEE Electron Device Lett.*, 17 (1996) 124; M. Arafa, K. Ismail, P. Fay, J.O. Chu, B.S. Meyerson and I. Adesida, *Electron. Lett.*, 31 (1995) 680.
- [7] U. Konig and F. Schaeffler, *IEEE Trans. Electron Device Lett.*, EDL-14 (1993) 205.
- [8] Y.H. Xie, D. Monroe, E.A. Fitzgerald, P.J. Silverman, F.A. Theil and G.P. Watson, *Appl. Phys. Lett.*, 63 (1993) 2263.
- [9] E.A. Fitzgerald, Y.H. Xie, D. Monroe, P.J. Silverman, J.M. Kuo, A.R. Kortan, F.A. Thiel and B.E. Weir, *J. Vac. Sci. Technol.*, B10 (1992) 1807.
- [10] H.H. Wieder, R.S. Goldman, J. Chen and A.P. Young, *J. Vac. Sci. Technol.*, B13 (1995) 1853; A.N. Chang, H.H. Wieder and W.S.C. Chang, *IEEE Photonics Technol. Lett.*, 7 (1995) 1159.
- [11] J.C. Bean, T.T. Sheng, L.C. Feldman, A.T. Fiory and R.T. Lynch, *Appl. Phys. Lett.*, 44 (1984) 102.
- [12] T.O. Sedgwick and D.A. Grützmacher, *J. Electrochem. Soc.*, 142 (1995) 2458.
- [13] D. Dutartre, P. Warren, I. Berbezier and P. Perret, *Thin Solid Films*, 222 (1992) 52.
- [14] B.S. Meyerson, *Appl. Phys. Lett.*, 48 (1986) 797.
- [15] K. Ismail, M. Arafa, K.L. Saenger, J.O. Chu and B.S. Meyerson, *Appl. Phys. Lett.*, 66 (1995) 1077.
- [16] K. Ismail, M. Arafa, F. Stern, J.O. Chu and B.S. Meyerson, *Appl. Phys. Lett.*, 66 (1995) 842.
- [17] F. Schaeffler, D. Tobben, H.J. Herzog, G. Abstreiter and B. Hollander, *Semicond. Sci. Technol.*, 7 (1992) 260.
- [18] Y.J. Mii, Y.H. Xie, E.A. Fitzgerald, D. Monroe, F.A. Theil and B.E. Weir, *Appl. Phys. Lett.*, 59 (1991) 1611.
- [19] M.M. Reiger and P. Vogl, *Phys. Rev. B*, 49 (1993) 14276.
- [20] R. Braunstein, A.R. Moore and F. Herman, *Phys. Rev.*, 109 (1958) 695.
- [21] K. Ismail, F.K. LeGoues, K.L. Saenger, M. Arafa, J.O. Chu, P.M. Mooney and B.S. Meyerson, *Phys. Rev. Lett.*, 73 (1994) 3447.
- [22] G. Abstreiter, H. Brugger, T. Wolf, H. Jorke and H.J. Herzog, *Phys. Rev. Lett.*, 54 (1985) 2441.
- [23] K. Ismail, B.S. Meyerson and P.J. Wang, *Appl. Phys. Lett.*, 58 (1991) 2117.
- [24] S.F. Nelson, K. Ismail, T.N. Jackson, J.J. Nocera, J.O. Chu and B.S. Meyerson, *Appl. Phys. Lett.*, 63 (1993) 794.
- [25] K. Ismail, *Solid State Phen.*, 47-48 (1996) 409.
- [26] F. Stern and S.E. Laux, *Appl. Phys. Lett.*, 61 (1992) 1110.
- [27] D. Monroe, Y.H. Xie, E.A. Fitzgerald, P.J. Silverman and G.P. Watson, *J. Vac. Sci. Technol. B*, 11 (1993) 1731.
- [28] R.M. Feenstra, M.A. Lutz, F. Stern, K. Ismail, P.M. Mooney, F.K. LeGoues, C. Stanis, J.O. Chu and B.S. Meyerson, *J. Vac. Sci. Technol. B*, 13 (1995) 1608.
- [29] R.M. Feenstra and M.A. Lutz, *J. Appl. Phys.*, 78 (1995) 6091.
- [30] K. Ismail, *personal communication*, 1996.
- [31] K. Ismail, F. Nelson, J.O. Chu and B.S. Meyerson, *Appl. Phys. Lett.*, 63 (1993) 660.
- [32] A. Sadek and K. Ismail, *Solid State Electron.*, 38 (1995) 1731.
- [33] D.V. Lang, R. People, J.C. Bean and A.M. Sergeant, *Appl. Phys. Lett.*, 47 (1985) 1333.
- [34] K. Ismail, J.O. Chu and B.S. Meyerson, *Appl. Phys. Lett.*, 64 (1994) 3124.
- [35] J.H. Van der Merwe, *J. Appl. Phys.*, 34 (1963) 117; J.H. Van der Merwe, *J. Appl. Phys.*, 34 (1963) 123.
- [36] J.W. Mathews and A.E. Blakesley, *J. Cryst. Growth*, 29 (1975) 273; J.W. Mathews and A.E. Blakesley, *J. Cryst. Growth*, 32 (1976) 265.
- [37] E.A. Fitzgerald, *Mater. Sci. Rep.*, 7 (1991) 87.
- [38] D. Hull and D.J. Bacon, *Introduction to Dislocations*, 3rd Edition, International Series on Materials Science and Technology, Vol. 37, Ch. 3, Pergamon, New York, 1984.
- [39] C.G. Tuppen and C.J. Gibbings, *J. Appl. Phys.*, 68 (1990) 1526.
- [40] D.C. Houghton, *Appl. Phys. Lett.*, 57 (1990) 2124.
- [41] R. Hull, J.C. Bean, D. Bahnck, L.J. Peticolas, Jr., K.T. Short and F.C. Unterwald, *J. Appl. Phys.*, 70 (1991) 2052.
- [42] R. Hull and J.C. Bean, *Phys. Stat. Solidi. (a)*, 138 (1993) 533.
- [43] W. Dodson and J.Y. Tsao, *Appl. Phys. Lett.*, 51 (1987) 1325.
- [44] J.P. Hirth and J. Lothe, *Theory of Dislocations 2nd Edition*, Ch. 15, Kreiger Publishing, Malabar, FL, 1992.
- [45] M.H. Grabow and G.H. Gilmer, *Mater. Res. Soc. Symp. Proc.*, 94 (1987) 15.
- [46] P.M.J. Maree et al., *J. Appl. Phys.*, 62 (1987) 4413.
- [47] R. Hull and J.C. Bean, *J. Vac. Sci. Technol.*, A7 (1989) 2580.
- [48] E.A. Fitzgerald et al., *J. Appl. Phys.*, 65 (1989) 2220.
- [49] D.J. Eaglesham et al., *Philos. Mag.*, 59 (1989) 1059.
- [50] S.V. Kamut and J.P. Hirth, *J. Appl. Phys.*, 67 (1990) 6844.

- [51] D.D. Perovic and D.C. Houghton, *Mater. Res. Soc. Symp. Proc.*, **263** (1992) 391.
- [52] W. Hagen and W. Strunk, *J. Appl. Phys.*, **17** (1978) 85.
- [53] F.K. LeGoues, B.S. Meyerson, J.F. Morar and P.D. Kirchner, *J. Appl. Phys.*, **71** (1992) 4230; F.K. LeGoues, B.S. Meyerson and F.J. Morar, *Phys. Rev. Lett.*, **66** (1991) 2903.
- [54] M.A. Capano, *Phys. Rev. B*, **45** (1992) 11768.
- [55] B.J. Spencer, P.W. Voorhees and S.H. Davis, *Phys. Rev. Lett.*, **67** (1991) 3696.
- [56] B.G. Orr, D. Kessler and C.W. Snyder, *Europhys. Lett.*, **19** (1992) 33.
- [57] W.H. Yang and D.J. Srolovitz, *Phys. Rev. Lett.*, **71** (1993) 1593.
- [58] J. Tersoff and F.K. LeGoues, *Phys. Rev. Lett.*, **72** (1994) 3570.
- [59] D.E. Jesson, S.J. Pennycook, J.-M. Baribeau and D.C. Houghton, *Phys. Rev. Lett.*, **71** (1993) 1744.
- [60] B.S. Meyerson, K.J. Uram and F.K. LeGoues, *Appl. Phys. Lett.*, **53** (1988) 2555.
- [61] F.K. LeGoues, *Phys. Rev. Lett.*, **72** (1994) 876.
- [62] D.J. Eaglesham et al., *Phys. Rev. Lett.*, **64** (1990) 1943.
- [63] M.A. Lutz, R.M. Feenstra, P.M. Mooney, J. Tersoff and J.O. Chu, *Surf. Sci.*, **316** (1994) L1075.
- [64] M.A. Lutz, R.M. Feenstra, F.K. LeGoues, P.M. Mooney and J.O. Chu, *Appl. Phys. Lett.*, **66** (1995) 724.
- [65] S.Y. Shiryayev, F. Jensen and J.W. Petersen, *Appl. Phys. Lett.*, **64** (1994) 3305.
- [66] D. Dutartre, P. Warren, F. Provenier, F. Chollet and P. Péro, *J. Vac. Sci. Technol. A*, **12** (1994) 1009.
- [67] G.P. Watson, E.A. Fitzgerald, Y.H. Xie and D. Monroe, *J. Appl. Phys.*, **75** (1994) 263.
- [68] G. Kissinger, T. Morgenstern, G. Morgenstern and H. Richter, *Appl. Phys. Lett.*, **66** (1995) 2083.
- [69] G.P. Watson, E.A. Fitzgerald, Y.H. Xie, P.J. Silverman, A.E. White and K.T. Short, *Appl. Phys. Lett.*, **63** (1993) 746.
- [70] M.A.G. Halliwell, *Inst. Phys. Conf. Ser.*, **60** (1981) 271.
- [71] P.F. Fewster, *Semicond. Sci. Technol.*, **8** (1993) 1915.
- [72] P.M. Mooney, J.L. Jordan-Sweet, G.B. Stephenson, F.K. LeGoues and J.O. Chu, *Advances in X-ray Analysis*, **38** (1993) 181.
- [73] F.K. LeGoues, P.M. Mooney and J.O. Chu, *Appl. Phys. Lett.*, **62** (1993) 140.
- [74] P.M. Mooney, F.K. LeGoues, J. Tersoff and J.O. Chu, *J. Appl. Phys.*, **75** (1994) 3968.
- [75] F.K. LeGoues, P.M. Mooney and J. Tersoff, *Phys. Rev. Lett.*, **71** (1993) 396.
- [76] P.M. Mooney, F.K. LeGoues and D. Grützmacher, unpublished.
- [77] F.K. LeGoues, unpublished.
- [78] Y. Chen, Z. Liliental-Weber, J. Washburn, J.F. Klem and J.Y. Tsao, *Appl. Phys. Lett.*, **66** (1995) 499.
- [79] K.L. Kavanagh, R.S. Goldman and C.P. Chang, *Scanning Microscopy*, **8** (1994) 905.
- [80] P.M. Mooney, F.K. LeGoues and J.L. Jordan-Sweet, *Appl. Phys. Lett.*, **65** (1994) 2845.
- [81] A.G. Cullis, D.J. Robbins, S.J. Barnett and A. Pidduck, *J. Vac. Sci. Technol.*, **A12** (1994) 1924.
- [82] J.L. Jordan-Sweet, P.M. Mooney, M.A. Lutz, R.M. Feenstra, J.O. Chu and F.K. LeGoues, *J. Appl. Phys.*, **80** (1996) 89.
- [83] J.L. Jordan-Sweet, P.M. Mooney and G.B. Stephenson, *Mater. Res. Soc. Symp.*, **375** (1995) 201.
- [84] P.M. Mooney, F.K. LeGoues, J.O. Chu and S.F. Nelson, *Appl. Phys. Lett.*, **62** (1993) 3464.
- [85] E. Koppensteiner, P. Hamberger, G. Bauer, V. Holý and E. Kasper, *Appl. Phys. Lett.*, **64** (1994) 172.
- [86] E. Koppensteiner, A. Schuh, G. Bauer, V. Holý, G.P. Watson and E.A. Fitzgerald, *J. Phys. D: Appl. Phys.*, **28** (1995) A114.
- [87] V. Holý, J.H. Li, G. Bauer, F. Schäffler and H.-J. Herzog, *J. Appl. Phys.*, **78** (1995) 5013.
- [88] P.M. Mooney, J.L. Jordan-Sweet, K. Ismail, J.O. Chu, R.M. Feenstra and F.K. LeGoues, *Appl. Phys. Lett.*, **67** (1995) 2373.
- [89] P.M. Mooney, J.L. Jordan-Sweet, J.O. Chu and F.K. LeGoues, *Appl. Phys. Lett.*, **66** (1995) 3642.
- [90] J.H. Li, E. Koppensteiner, G. Bauer, M. Hohnisch, H.-J. Herzog and F. Schäffler, *Appl. Phys. Lett.*, **67** (1995) 223.
- [91] J.H. Li, V. Holý, G. Bauer, J.F. Nützel and G. Abstreiter, *Appl. Phys. Lett.*, **67** (1995) 789.
- [92] H.J. Leamy, *J. Appl. Phys.*, **53** (1982) R51.
- [93] J.W.P. Hsu, E.A. Fitzgerald, Y.H. Xie, P.J. Silverman and M.J. Cardillo, *Appl. Phys. Lett.*, **61** (1992) 1293.
- [94] P.M. Mooney, F.H. Dacol, J.C. Tsang and J.O. Chu, *Appl. Phys. Lett.*, **62** (1993) 2069.
- [95] J.C. Tsang, P.M. Mooney, F. Dacol and J.O. Chu, *J. Appl. Phys.*, **75** (1994) 8098.
- [96] Y.H. Xie, G.H. Gilmer, C. Roland, P.J. Silverman, S.K. Buratto, J.Y. Cheng, E.A. Fitzgerald, A.R. Kortan, S. Schuppler, M.A. Marcus and P.H. Citrin, *Phys. Rev. Lett.*, **73** (1994) 3006.
- [97] J.W.P. Hsu, E.A. Fitzgerald, Y.H. Xie and P.J. Silverman, *Appl. Phys. Lett.*, **65** (1994) 344.
- [98] F.M. Ross, R. Hull, D. Bahnck, J.C. Bean, L.J. Peticolas, R.A. Hamm and H.A. Huggins, *J. Vac. Sci. Technol. B*, **10** (1992) 2008.
- [99] J.R. Chelikowsky, *Phys. Rev. Lett.*, **49** (1982) 1569.
- [100] J.R. Chelikowsky and J.C.H. Spence, *Phys. Rev. B*, **30** (1984) 694.
- [101] V.V. Bulatov, S. Yip and A.S. Argon, *Philos. Mag. A*, **72** (1995) 453.
- [102] K. Masuda-Jindo, *Mater. Sci. Forum*, **83–87** (1992) 1333.
- [103] Y.M. Huang, J.C.H. Spence and O.F. Sankey, *Phys. Rev. Lett.*, **74** (1995) 3392.
- [104] S. Öberg, P.K. Stick, R. Jones and M.I. Heggie, *Phys. Rev. B*, **51** (1995) 13138.
- [105] L.P. Tilly, P.M. Mooney, J.O. Chu and F.K. LeGoues, *Appl. Phys. Lett.*, **67** (1995) 2488.
- [106] J. Weber and M.I. Alonso, *Phys. Rev. B*, **40** (1989) 5683.
- [107] K. Weronek, J. Weber, A. Höpner, F. Ernst, R. Buchner, M. Stefaniak and H. Alexander, *Mater. Sci. Forum*, **83–87** (1992) 1315.
- [108] R. Sauer, J. Weber, J. Stolz, E.R. Weber, K.-H. Kusters and H. Alexander, *Appl. Phys. A*, **36** (1985) 1.
- [109] G.S. Mitchard and T.C. McGill, *Phys. Rev. B*, **25** (1982) 5351.

- [110] J.C. Sturm, H. Manoharan, L.C. Lenchushyn, M.L.W. Thewalt, N.L. Rowell, J.-P. Noël and D.C. Houghton, *Phys. Rev. Lett.*, **66** (1991) 1362.
- [111] J.C. Sturm, X. Xiao, P.V. Schwartz, C.W. Liu, L.C. Lenchushyn and M.L.W. Thewalt, *J. Vac. Sci. Technol., B* **10** (1992) 1998.
- [112] G. Bremond, A. Souifi, T. Benyattou and D. Dutartre, *Thin Solid Films*, **222** (1992) 60.
- [113] K. Terashima, T. Ikarashi, D. Tweet, K. Miyana, T. Tatsumi and M. Tajima, *Appl. Phys. Lett.*, **65** (1994) 601.
- [114] P.O. Hansson, J.H. Werner, L. Tapfer, L.P. Tilly and E. Bauser, *J. Appl. Phys.*, **68** (1990) 2158.
- [115] V. Higgs, E.C. Lightowers, E.A. Fitzgerald, Y.H. Xie and P.J. Silverman, *J. Appl. Phys.*, **73** (1993) 1952.
- [116] J. Michel, E.A. Fitzgerald, Y.-H. Xie, P.J. Silverman, M. Morse and L.C. Kimerling, *J. Electron. Mater.*, **21** (1992) 1099.
- [117] A. Souifi, G. Bremond, T. Benyattou, G. Guillot, D. Dutartre and I. Berbezier, *J. Vac. Sci. Technol. B*, **10** (1992) 2002.
- [118] H.B. Erzgräber, G. Kissinger, G. Morganstern and Th. Morganstern, *Solid State Phen.*, **47–48** (1996) 529.
- [119] V. Higgs, E.C. Lightowers, C.E. Norman and P. Knightley, *Mater. Sci. Forum*, **83–87** (1992) 1309.
- [120] V. Nagesh, H.G. Grimmeiss, E.-L. Heliqvist, K.L. Ljutovich and A.S. Ljutovich, *Semicond. Sci. Technol.*, **5** (1990) 566.
- [121] P.N. Grillo, S.A. Ringel, E.A. Fitzgerald, G.P. Watson and Y.H. Xie, *J. Appl. Phys.*, **77** (1995) 3248.
- [122] P.N. Grillo, S.A. Ringel, E.A. Fitzgerald, G.P. Watson and Y.H. Xie, *J. Appl. Phys.*, **77** (1995) 676.
- [123] W. Staiger, G. Pfeiffer, K. Weronek, A. Höpner and J. Weber, *Mater. Sci. Forum*, **143–147** (1994) 1571.
- [124] L.C. Kimerling and J.R. Patel, *Appl. Phys. Lett.*, **34** (1979) 73.
- [125] L.C. Kimerling, J.R. Patel, J.L. Benton and P.E. Freeland, *Inst. Phys. Conf. Ser.*, **59** (1981) 401.
- [126] J.C. Brighten, I.D. Hawkins, A.R. Peaker, R.A. Kubiak, E.H.C. Parker and T.E. Wall, *J. Appl. Phys.*, **76** (1994) 4237.
- [127] P. Bhattacharya, S.-H. Li, J. Lee and S. Smith, *Mater. Res. Soc. Symp. Proc.*, **325** (1994) 147.
- [128] P.M. Mooney, L.P. Tilly, C.P. D'Emic, J.O. Chu and F. Cardone, *J. Appl. Phys.*, submitted.
- [129] P. Omling, E.R. Weber, L. Montelius, H. Alexander and J. Michel, *Phys. Rev. B*, **32** (1985) 6571.